

## Research Paper

# Complex Ice Chemistry: A comparative study of electron irradiated planetary ice analogues containing methane

Kristina A. Kipfer<sup>a,b,\*</sup>, André Galli<sup>a</sup>, Andreas Riedo<sup>a,b</sup>, Marek Tulej<sup>a</sup>, Peter Wurz<sup>a,b</sup>, Niels F.W. Ligterink<sup>a,b</sup>

<sup>a</sup> Space Research and Planetary Sciences, Physics Institute, University of Bern, Sidlerstrasse 5, Bern, 3012, Switzerland

<sup>b</sup> NCCR PlanetS, University of Bern, Bern, 3012, Switzerland



## ARTICLE INFO

## Keywords:

Ices  
Experimental techniques  
Kuiper belt  
Comets

## ABSTRACT

Various Solar System objects are covered in layers of ice that are dominated by H<sub>2</sub>O, CH<sub>4</sub>, and N<sub>2</sub> and in which complex chemical processes take place. In this work, the influence of composition and irradiation duration on the volatile irradiation products of mixed CH<sub>4</sub>:N<sub>2</sub>, CH<sub>4</sub>:H<sub>2</sub>O, and CH<sub>4</sub>:H<sub>2</sub>O:N<sub>2</sub> ices after electron irradiation are studied. The ices were irradiated for 2 or 4 h with 5 keV electrons, followed by a temperature programmed desorption, where the desorption of the volatile irradiation products was observed. The formation of C<sub>2</sub>H<sub>x</sub> and C<sub>3</sub>H<sub>x</sub> is observed in all ices and for both irradiation times. For the ices containing H<sub>2</sub>O, molecules as large as tentatively identified C<sub>4</sub>H<sub>x</sub> and C<sub>5</sub>H<sub>x</sub> are observed to co-desorb with water, whereas for CH<sub>4</sub>:N<sub>2</sub> a continuous desorption signal is observed instead of a sharp desorption peak. A decrease in signal intensity from the 2 to the 4 h irradiation is observed for most *m/z* signals in CH<sub>4</sub>:H<sub>2</sub>O and CH<sub>4</sub>:H<sub>2</sub>O:N<sub>2</sub> ices, whereas the opposite is recorded for CH<sub>4</sub>:N<sub>2</sub>, where in general larger signal for longer irradiation duration is seen. The addition of nitrogen to the CH<sub>4</sub>:H<sub>2</sub>O ice did not lead to clear identification of different molecules, but instead to a decrease of the observed signal for complex molecules, suggesting that the addition of nitrogen to the CH<sub>4</sub>:H<sub>2</sub>O mixture primarily leads to a more effective incorporation of material in an organic residue. The analysis of the residue will be subject of future work to complement the findings in this study.

## 1. Introduction

Ice can be found ubiquitously in the universe: On the surface of interstellar or circumplanetary dust grains, in comets, and on planetary surfaces in the solar system (Boogert et al., 2015; Altwegg et al., 2019). These ices can get energetically processed, for example by irradiation via electrons, which is hypothesized to be a major pathway in the formation of molecules (Mason et al., 2014). In the case of Galilean icy satellites, electron irradiation dominates the energy flux into the surface (Cooper et al., 2001). Similarly, for Kuiper belt objects (KBO), the lack of a significant magnetosphere means that KBOs are easily exposed to irradiation by charged particles, both from the solar wind as well as from cosmic rays. Energetic electrons are an important component of cosmic rays, solar wind, and planetary magnetospheric plasmas (Cooper et al., 2001; Arumainayagam et al., 2019). Furthermore, keV electrons may be used as proxies for galactic cosmic rays (e.g. Abplanalp et al., 2018; Marks et al., 2022) and the amount of energy deposited by ionizing radiation as a function of depth for keV electrons is comparable to the one of MeV ions (Ferrari et al., 2021). Energetic electrons are able to break bonds that UV photons are

not able to. For example, the energy of Lyman- $\alpha$  photons (121.6 nm or 10.2 eV) is insufficient to break certain bonds, such as in the case of CO. Other molecules, for example N<sub>2</sub>, do not absorb photons at Lyman- $\alpha$  wavelength (Wu et al., 2012). However, these bonds can be broken by incoming electrons with typical energies ranging from keV to MeV (e.g. Hudson et al., 2008; Materese et al., 2015).

Previous studies using electrons to irradiate interstellar or planetary ice analogs show the formation of a variety of products, some with potential importance for the emergence of life, such as dipeptides (Kaiser et al., 2013), as well as amino acids and their building blocks (Holtom et al., 2005; Kaiser et al., 2015; Förstel et al., 2017; Esmaili et al., 2018). A study on methanol ice showed that low-energy and high-energy electrons produce similar products (Sullivan et al., 2016). This could point to the fact that as electrons penetrate into ice, secondary electrons with energies of several tens of eV and low energy X-rays are generated, which themselves interact with the ice and induce further chemistry (Arumainayagam et al., 2019).

Solid water is one of the most abundant ices in astrophysical environments, not only on the surface of interstellar ice grains, but

\* Corresponding author at: Space Research and Planetary Sciences, Physics Institute, University of Bern, Sidlerstrasse 5, Bern, 3012, Switzerland.  
E-mail addresses: [kristina.kipfer@unibe.ch](mailto:kristina.kipfer@unibe.ch) (K.A. Kipfer), [niels.ligterink@unibe.ch](mailto:niels.ligterink@unibe.ch) (N.F.W. Ligterink).

also on the surface of various bodies in the solar system, such as on the moons Europa and Enceladus among many others (Gudipati and Cooper, 2013). Various laboratory studies have been conducted on the effect of energetic processing on water ice, including the formation of new species (Zheng et al., 2006), phase changes (Moore and Hudson, 2003; Zheng et al., 2009), and the desorption of various species over the course of the irradiation (Rowntree et al., 1991; Galli et al., 2018; Meier and Loeffler, 2020; Davis et al., 2021). In the solar system, major mixing components with water ice include carbon dioxide, methane, and nitrogen (Prockter, 2005).

Methane is suggested to be formed in interstellar ices, where hydrogen and carbon atoms combine (d'Hendecourt et al., 1985; Qasim et al., 2020) and has been detected in solid and gaseous form in the interstellar medium. Methane has been detected in comets (e.g., Brooke et al., 1996; Müller et al., 2022) in addition to other hydrocarbons such as ethane (C<sub>2</sub>H<sub>6</sub>, Mumma et al., 1996) and acetylene (C<sub>2</sub>H<sub>2</sub>, Brooke et al., 1996). Methane is also found on planetary bodies, including in the atmospheres of Mars, Jupiter, Saturn, Uranus, and Neptune. Furthermore, methane (and traces of other hydrocarbons) has been found on Titan (Coustenis et al., 2003) and on Triton (Hansen et al., 2021). Pluto, whose surface is dominated by N<sub>2</sub> ice, shows not only embedded methane, but also islands of solid methane (Douté et al., 1999). The surface of dwarf planet Eris has been suggested to contain solid methane and nitrogen ices (Tegler et al., 2010). Triton, a presumed captured KBO, is also suggested to possess a nitrogen rich surface composition, similar to Pluto (Quirico et al., 1999; Grundy et al., 2010). The interaction of the surface ice of KBOs with charged particles from the solar wind and cosmic rays is suggested to contribute to the color diversity observed for KBOs (Luu and Jewitt, 1996). Previous irradiation experiments on methane-rich ices have shown that hydrocarbons (C<sub>x</sub>H<sub>y</sub>) are among the major products (Bennett et al., 2006; Bossa et al., 2015). The irradiation of pure methane ices by energetic electrons has been shown to lead to the formation of complex hydrocarbons such as methylacetylene (CH<sub>3</sub>CCH) and propene (CH<sub>3</sub>CHCH<sub>2</sub>), which are thought to be precursors to polycyclic aromatic hydrocarbons (Abplanalp et al., 2019). Furthermore, irradiation of CH<sub>4</sub>:N<sub>2</sub>:CO ices with electrons has shown to lead to the formation of nitrogen containing molecules such as HCN (Kim and Kaiser, 2012).

To investigate the possible role the irradiation of ices play in the inventory of molecules on planetary surfaces or on the surface of comets, it is crucial to investigate not only which molecules are formed, but also to identify which molecules possibly desorb from planetary or cometary surfaces in the event of heating. Such heating could occur during an inward migration of a body or comet in the solar system or due to solar radiation (Morbidelli et al., 2016; Rubin et al., 2019). These molecules could possibly contribute to an atmosphere or to the coma of a comet, allowing for their detection via in situ measurements or in flybys.

To study the desorption of various molecules, temperature programmed desorption (TPD) experiments are often used (Ligterink et al., 2017; Ligterink et al., 2018). There, a sample surface is heated and the desorption of products from the surface as a function of the temperature is monitored, usually by using a quadrupole mass spectrometer (QMS) or similar equipment. However, attribution of the signals to certain chemical compounds is increasingly challenging the more components a sample includes, because multiple parent molecules can contribute to the same signal because of the electron ionization fragmentation pattern. Nevertheless, QMS data often gives valuable information on the desorption temperatures of various molecules and their interactions with each other in a mixture.

In this study, mixtures of CH<sub>4</sub>, H<sub>2</sub>O and N<sub>2</sub> ices are investigated after 2 and 4 h electron irradiation and the desorption of volatile irradiation products is studied using TPD data. The differences between the desorption trace as a function of ice composition and irradiation duration are noted and the influence and identification of major irradiation products is attempted. The desorption behavior of these irradiation products is compared and analyzed.

## 2. Methods

### 2.1. Experimental setup

The experiments are conducted in the ICEBEAR setup, which is a new laboratory setup to investigate the physical and chemical processes in interstellar and planetary ice analogs. The chamber and selected detail views are shown in Fig. 1, a schematic drawing in Fig. 2. The setup consists of a stainless steel vacuum chamber that is pumped by a turbomolecular pump (MAG W 400 iP, Leybold), backed by an oil-free roughing pump (ScrollVac SC 15 D, Leybold), reaching a base pressure in the order of  $\sim 10^{-8}$  mbar at room temperature, whereas a pressure below  $5 \cdot 10^{-9}$  mbar is reached when the cryostat is cooling. The pressure within the chamber is monitored using a PKR 261 pressure gauge (Pfeiffer Vacuum), read out with a TPG 252 A controller (Pfeiffer Vacuum). The chamber has two viewing ports, which allow for direct observation of the sample. A cluster flange is attached to one port of the chamber, where an electrical feedthrough, a manually operated valve for gas deposition, a pressure gauge and a QMS (QMG 250 M2, Pfeiffer Vacuum) are attached. The QMS can be used to analyze the residual gas in the chamber.

Ice samples are grown in situ on a copper sample holder ( $\varnothing$  5 cm), mounted on the cold head of a closed-cycle Helium cryostat (SRDK Series Cryocooler, Sumitomo Cryogenics), which allows for cooling of the sample holder down to  $\sim 5$  K. To ensure optimal thermal conductivity, an indium sheet is used between the sample holder and the cold head. Furthermore, to ensure proper cooling, a heat shield is mounted around the cold finger of the cryostat. The temperature of the sample holder is monitored via a Si diode (DT670-CU, Lakeshore) attached to the underside of the sample holder and recorded by a temperature controller (Lakeshore Model 336). Two heating rods are fixed to the sample holder, allowing for resistive heating of the sample holder via the temperature controller. The cryostat is attached to a stage (MB3006, McAllister) to move the sample holder in xyz direction. The sample holder can be removed from the chamber for post experiment ex situ analysis. All equipment and consumables going into the chamber are cleaned beforehand using Isopropanol (99.999% purity) and Milli-Q grade water (TOC < 5 ppb).

Gases are mixed within a separately pumped gas mixing backbone, which consists out of stainless steel crosspieces. The gas mixing backbone is pumped via a Turbopump (HiPace 80, Pfeiffer Vacuum), backed by an oil-free roughing pump (MV 2 NT, Vacuubrand). The pressure within the gas mixing backbone is monitored using a capacitance diaphragm pressure gauge (CMR 362, Pfeiffer Vacuum), which measures pressures independent of gas species. Two gas bottles and a vial with a liquid can be attached to the backbone, each connection with its own valve to the backbone. The gas mixing system is connected to the main chamber by a manually operated leak valve, which is used to deposit the gas mixture into the chamber.

An electron gun (EGG-3103, Kimball Physics) is mounted on top of the chamber for this study, allowing for a working distance of about 400 mm between electron gun and sample holder surface and irradiation at an incidence angle of 0° relative to the sample surface normal. The target is irradiated with electrons at a fixed energy, which can be selected in a range from 0.1 keV to 10 keV. The spot size of the electron gun can be adjusted and allows for spot diameters in the range of 5 to  $\geq 30$  mm. At this working distance, typical currents on the sample holder surface from  $\sim 0.1$   $\mu$ A to several  $\mu$ A can be achieved.

#### 2.1.1. Sample preparation

To grow ice on the sample holder, the gases are mixed at the desired ratios by pressure in the gas mixing backbone and leaked into the chamber via a manually operated mechanical leak valve. The gas mixtures condense onto the copper sample holder, which has been cooled down to the deposition temperature using the cryostat and resistive heating.

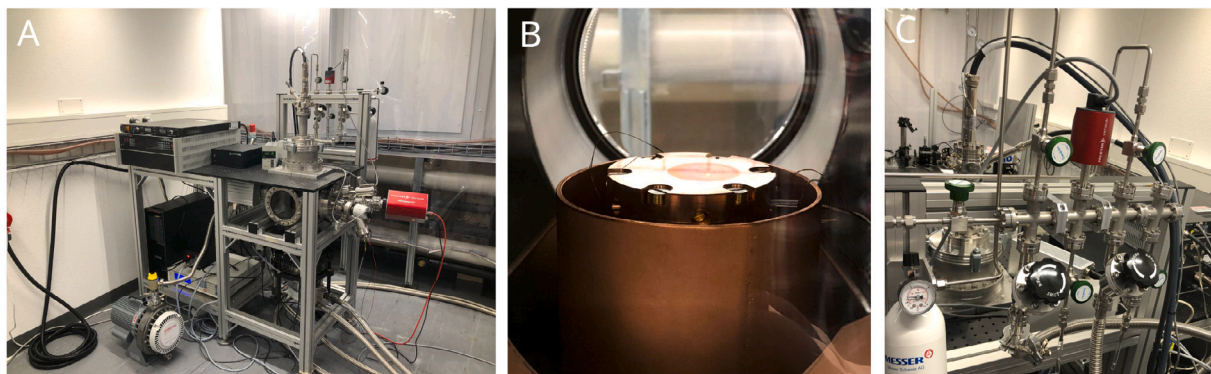


Fig. 1. Images showing the instrument and relevant parts. For the labels, refer to Fig. 2.

A: The ICEBEAR setup.

B: The inside of the main chamber as seen through the view port, showing the sample holder after an irradiation experiment with a residue on the surface. The heat shield around the sample holder can be seen as well.

C: The gas mixing system.

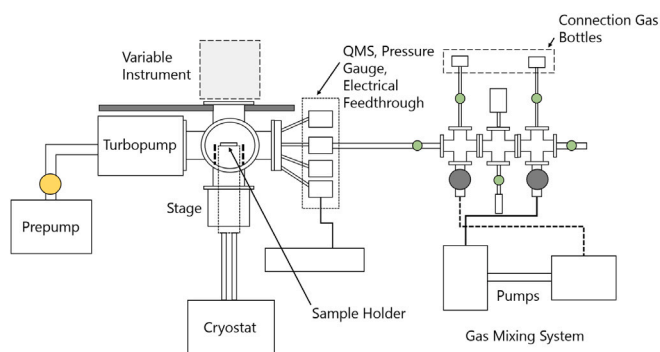


Fig. 2. A schematic drawing of ICEBEAR as used for this study. Shown are the two parts of the setup, the main chamber and the gas mixing system. Important parts of the setup are labeled. For the experiments presented in this work, an electron gun was used in the spot labeled “Variable Instrument”, further described in Section 2.1.2.

The ice thickness is not monitored *in situ*, but is calculated by assuming that a leak rate of  $10^{-6}$  torr  $s^{-1}$  corresponds to 1 langmuir (L) of material on the sample holder surface (Renner, 2007). We assume that 1 L can be approximated as 1 monolayer (ML) of material on the sample holder surface.

For this study, different mixtures of  $H_2O$  (Milli-Q, TOC < 5 ppb),  $CH_4$  (Messer 99.995%), and  $N_2$  (Messer, 99.999%) ices have been studied to investigate the influence of each component on the volatile irradiation products and the desorption behavior of these products. The ratios of the parent mixed ices in the backbone are  $CH_4:H_2O \sim 1:1$ ,  $CH_4:N_2 \sim 4:1$ , and  $CH_4:H_2O:N_2 \sim 4:4:1$ .

The gases are mixed within the backbone at the desired ratio and are then deposited at a pressure of  $4 \cdot 10^{-6}$  mbar for 1500 s, leading to the formation of an ice layer with a thickness of 4500 ML. The sample holder is kept at a constant temperature of 20 K during the deposition. A calculation of the thickness of the ices for 4500 ML led to an estimate for pure  $CH_4$  ( $\rho = 0.53$  g  $cm^{-3}$  (Wyckoff and Wyckoff, 1965; Bennett et al., 2006)) of at least  $\sim 1.7$   $\mu m$ , for pure amorphous  $H_2O$  ( $\rho = 0.94$  g  $cm^{-3}$  (Angell, 2004; Jones et al., 2014)) of  $\sim 1.2$   $\mu m$ , and for pure  $N_2$  ( $\rho = 0.94$  g  $cm^{-3}$  (Satorre et al., 2008)) of 0.7  $\mu m$ . Note here that for mixed ices, a ratio-weighted average is assumed for the densities and the thickness of the ices.

### 2.1.2. Electron irradiation

The details of each experiment performed during this study are collected in Table 1.

The gas mixtures adsorb onto the cooled down sample holder at  $T = 20$  K and are subsequently irradiated with 5 keV electrons from the

Table 1

Experiments conducted on 4500 ML of various ice mixtures, containing  $CH_4$ ,  $H_2O$ , and/or  $N_2$  deposited at 20 K on the sample holder. The values in the second to fourth columns correspond to the pressure ratios of gases used to make the initial mixture in the gas mixing backbone. Please note that the pumping is less efficient for  $N_2$  compared to the other species present, therefore it is assumed that the backbone ratio of nitrogen is a lower limit for the ratio in the ice. For each experiment, a TPD from 20–300 K was performed. Please note that for the experiments containing water, the gas mixtures had to be prepared in two batches to deposit the amount needed, but was consistent between irradiation and respective blank experiment. The prescript *B* refers to the “Blank” experiments, for which no irradiation was performed. Experiments with a prescript *S* were Supplementary experiments, which were designed to test the system and results from these experiments are not presented in the main body of the text, but are available in part in the appendix, see Fig. B.16. Furthermore, the dose was not calculated for these experiments. Please note that the biggest uncertainty in the experiment originates from the current of the electron gun, which could not be measured *in situ* and instead had to be measured and calibrated before the experiment series. The uncertainty of the current of the electron gun is about  $\pm 10\%$ . The errors have been calculated via Gaussian error propagation.

Experiment	$H_2O$	$CH_4$	$N_2$	Fluence [ $e^{-1} cm^{-2}$ ]	Dose [ $eV molec^{-1}$ ]
BO	–	–	–	–	–
BI	1	1	–	–	–
I	1	1	–	$(8.5 \pm 1.2) \cdot 10^{15}$	$28.46 \pm 0.65$
II	1	1	–	$(1.7 \pm 0.2) \cdot 10^{16}$	$56.92 \pm 0.65$
BIII	4	4	1	–	–
III	4	4	1	$(8.5 \pm 1.2) \cdot 10^{15}$	$28.35 \pm 0.65$
IV	4	4	1	$(1.7 \pm 0.2) \cdot 10^{16}$	$56.70 \pm 0.65$
BIII	–	4	1	–	–
V	–	4	1	$(8.5 \pm 1.2) \cdot 10^{15}$	$28.39 \pm 0.65$
VI	–	4	1	$(1.7 \pm 0.2) \cdot 10^{16}$	$56.78 \pm 0.65$
SI	4	–	1	$(8.5 \pm 1.2) \cdot 10^{15}$	–
SII	4	–	1	–	–
SIII	1	–	–	$(8.5 \pm 1.2) \cdot 10^{15}$	–

electron gun. The ices are irradiated for a duration of 2 or 4 h at a current of  $\sim 1$   $\mu A$ . The diameter for the spot size has been measured to be  $\sim 26 \pm 3$  mm and has been kept constant over the measurement series.

As a simultaneous usage of a Faraday cup with the sample holder was not possible with the current setup, the current was measured at the beginning of the measurement series and the settings corresponding to a 1  $\mu A$  current on the Faraday cup were noted and consequently applied for further measurement series. This approach introduces uncertainties in determining the current on the surface of the sample holder, which is  $\pm 10\%$ . For further information on the current measurements, see Figs. A.12 and A.13 in the Appendix A.

The irradiated area was determined to be  $5.3 \pm 0.5$   $cm^2$ , which led to an approximated electron flux of

$$\phi_{5 \text{ keV}} = \frac{I}{e \cdot A} = (1.2 \pm 0.2) \cdot 10^{12} e^{-1} s^{-1} cm^{-2}$$

**Table 2**

Values used in Eq. (1) to calculate the dose each of the ices receives during the irradiation.

Variable	Physical Meaning	Irradiated ice		
		CH <sub>4</sub> :N <sub>2</sub>	CH <sub>4</sub> :H <sub>2</sub> O	CH <sub>4</sub> :H <sub>2</sub> O:N <sub>2</sub>
$E_{init}$	Initial kinetic energy of electrons	5 keV $\pm$ 0.01 keV		
$I$	Irradiation current	1 $\mu$ A $\pm$ 10%		
$A$	Irradiated area	5.3 $\pm$ 0.5 cm <sup>2</sup>		
$\rho^a$	Density of the ice [g cm <sup>-3</sup> ]	0.61 $\pm$ 0.06	0.74 $\pm$ 0.07	0.72 $\pm$ 0.07
$E_{bs}^b$	Average kinetic energy of backscattered electrons [keV]	2.81 $\pm$ 1.20	2.80 $\pm$ 1.21	2.80 $\pm$ 1.20
$f_{bs}^b$	Fraction of backscattered electrons	0.0441	0.0371	0.0461
$E_{trans}^b$	Average kinetic energy of transmitted electrons [keV]	0	0	0
$f_{trans}^b$	Fraction of transmitted electrons	0	0	0
$L^b$	Average penetration depth [nm]	727.1 $\pm$ 201.4	556.5 $\pm$ 148.3	612.3 $\pm$ 170.9

<sup>a</sup>The values for the densities of the mixed ices were calculated using a weighted value for the densities of the parent ices. For more details, see Section 2.1.1. The uncertainty of this method has been estimated with 10%.

<sup>b</sup>These values are derived from the CASINO simulation, run with the parameters listed in this table. Whenever an error is given, the standard deviation is calculated.

The error was calculated using Gaussian error propagation and taking the estimated uncertainty of the electron gun current as 10%.

For such a flux and under the present conditions, any changes within the ice due to macroscopic heating effects are likely insignificant (Mif-[sud et al., 2021](#)). For the measurements, this corresponds to a fluence of electrons for the two irradiation durations of  $\sim 8.5 \cdot 10^{15} \text{ e}^- \text{ cm}^{-2}$  (2 h) and  $\sim 1.7 \cdot 10^{16} \text{ e}^- \text{ cm}^{-2}$  (4 h) respectively. The interaction of the electrons with the ice was simulated with the CASINO software ([Drouin et al., 2007](#)) and results showed, that the average penetration depth for the electrons is below the ice thickness of the ices calculated in Section 2.1.1, therefore interaction with the sample holder surface is assumed to be negligible. Furthermore, the software is used to obtain the parameters for the dose per molecule ( $D$ ), which are collected in [Table 2](#) and is calculated using the following equation ([Förstel et al., 2016](#)):

$$D = \frac{I \cdot t \cdot m}{e \cdot N_A \cdot \rho \cdot A \cdot L} (E_{init} - f_{trans} E_{trans} - f_{bs} E_{bs}) \quad (1)$$

An estimated dose on the surface of KBOs is  $\sim 10 \text{ eV}$  per molecule after  $10^8$  years ([Cooper et al., 2003](#); [Zheng and Kaiser, 2010](#)), therefore our two sets of irradiation experiments simulate processing of KBO ices in the order of  $2.5 \cdot 10^8$  and  $5 \cdot 10^8$  years respectively.

Over the course of the irradiation, the ice is monitored with the QMS to observe any non-thermal desorption products. The only prominent signal can be observed for  $m/z = 2$ , most likely H<sub>2</sub>. However, one has to be aware that multiple sources might contribute to this signal increase, such the heating and outgassing of the electron gun filament.

## 2.2. TPD-QMS data analysis

After the irradiation by electrons, the ice is kept isothermally at the deposition temperature of 20 K for an hour before the ice is warmed up to 300 K at a constant heating rate of 2 K min<sup>-1</sup>. During the warm up, the desorption signals are monitored with the QMS, which scans the masses from 1–100 amu at an ionization energy of 70 eV. A dwell time of 32 ms for all masses with an electron current of 2000  $\mu$ A was used for all experiments. The signal recorded during the TPD corresponds to signal coming from both the irradiated and the non-irradiated part of the sample holder, as well as possible contribution from the surrounding environment due to the deposition method. Especially for the masses corresponding to the fragmentation pattern of the main ice components, the signal is likely dominated by the non-irradiated part. However, subtracting the blank measurements allows for a better distinction between the irradiated and the non-irradiated area. It must further be noted that it is not possible to distinguish the molecules formed during the irradiation from the molecules formed via other thermally induced mechanisms during the TPD using mass spectrometry ([Bennett and Kaiser, 2007](#)), such as for example formation of molecules due to recombination of radicals, which become mobile during the warm up.

For potential further analysis and cleaning, the sample holder can be removed from the chamber after completion of the measurement.

## 2.2.1. Data preparation and processing

The data displayed in the subsequent sections are either the raw data, which is the signal measured by the QMS, synchronized with the temperature measured with the diode, or processed data. Which set of data is used is indicated in the figure captions or in the text. Briefly, for processed data, the TPD spectra are baseline corrected using an adaptive iterative reweighted penalized least squares method ([Zhang et al., 2010](#)) and a python built-in method for a Butterworth filter for data filtering. Afterwards, the data are analyzed using a combination of the built-in python scipy find\_peaks function ([Jones et al., 2001](#)) and the argrextrema function ([Virtanen et al., 2020](#)). The detected peaks are then fitted using an iterative fit with Gaussian functions centered at the peak location. Care has been taken to ensure proper peak detection, however, in spectra with a large range in signal amplitude, such as is the case for  $m/z = 28$ , low amplitude peaks are sometimes obscured by signal originating a lingering desorption of the main desorption event, see the data for  $m/z = 28$  in [Fig. B.15](#) for example.

## 3. Results and discussion

The measurements conducted in this study are summarized in [Table 1](#). An overview of the obtained TPD data is shown in [Fig. 3](#). This heatmap makes use of the raw data without blank correction and therefore also shows contributions from the non-irradiated part of the sample holder during the TPD, which is most noticeable for the main mass peaks of the parent ices. Prominent desorption events occur at around 30 K for N<sub>2</sub>, 40 K for CH<sub>4</sub>, and 175 K for H<sub>2</sub>O. These are in agreement with previous desorption studies of these molecules (e.g., [Collings et al., 2004](#)). Besides the parent ice species, a significant signal is seen in the  $m/z = 2$  channel at temperatures of  $\leq 50$  K. This is H<sub>2</sub>, which is readily formed during the irradiation of the ices as well as from any of the other closed shell species such as CH<sub>4</sub> and H<sub>2</sub>O due to the dissociation and recombination reactions induced in the QMS.

To further investigate the irradiation products and their desorption temperatures, trends in the peak desorption temperatures have been analyzed, the result of which can be seen in [Fig. 4](#). Here the blank corrected data have been used, meaning that the signal of the unprocessed ices are subtracted. In this figure each data point indicates the peak desorption temperature of a peak detected in a certain mass-over-charge channel. Multiple desorption peaks can be present in the same mass-over-charge channel. This makes it easy to see trends and connect fragments of desorbing molecules together. Furthermore, each node is color coded according to the area of the Gaussian fit of the peak, which makes it possible to assess the intensity of the desorption signal in this plot and to retrieve fragmentation patterns.

Finally, [Fig. 5](#) shows the integrated desorption signals for the temperature regimes from 60 to 130 K and 130 to 200 K and for the mass-over-charge ranges of  $m/z = 20\text{--}49$  and  $m/z = 50\text{--}72$ . For each experiment, the top two panels show the masses in the two (red) and

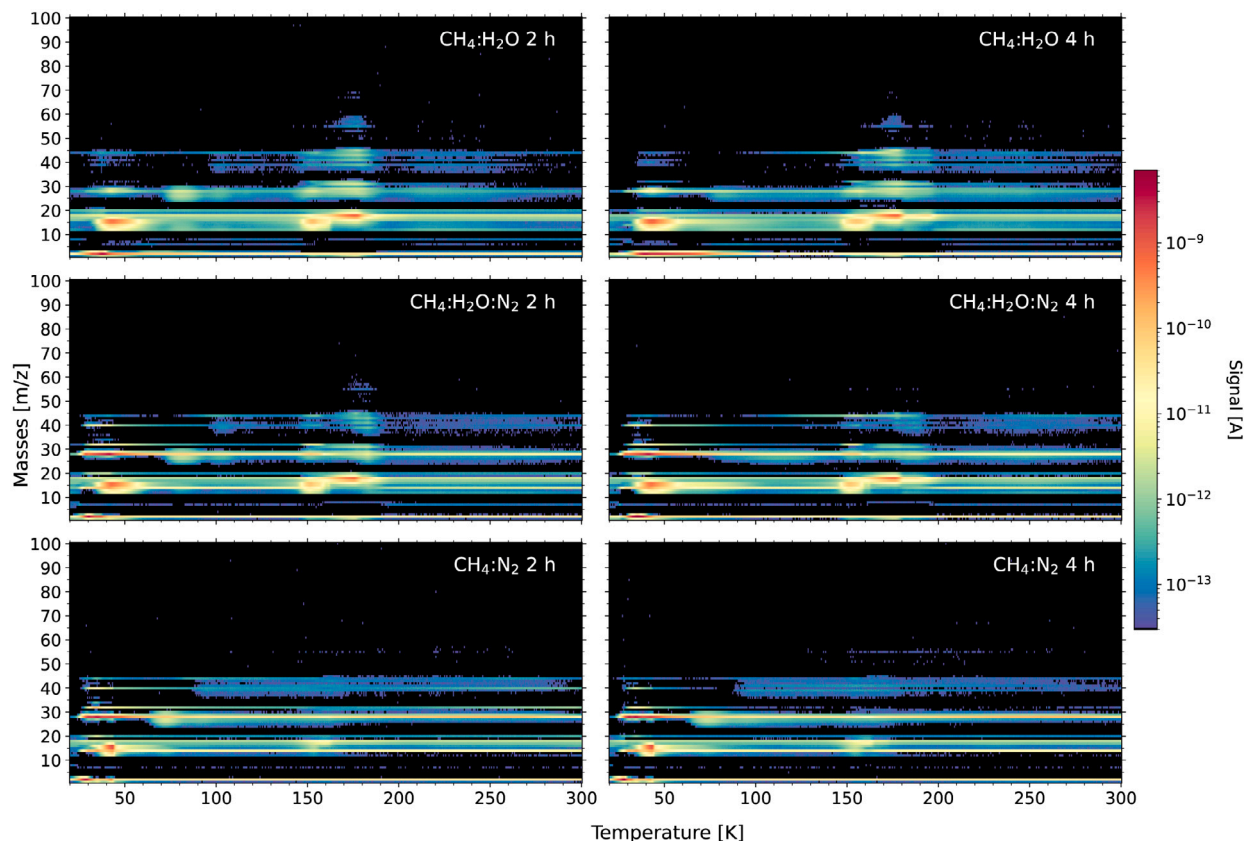


**Fig. 3.** A compilation of the TPD results of the irradiated ices in the form of a heatmap. The plot shows the signal detected by the QMS as a function of the  $m/z$  and the temperature during the TPD. The data have been filtered to show signal above a noise threshold, which has been defined as the largest signal for  $m/z = 96$ , which has manually been checked to ensure that it does not contain any significant signal. The plots show two prominent desorption regimes, the methane/nitrogen desorption below 50 K and the water desorption at  $\sim 180$  K, if applicable. Especially during the water desorption, prominent codesorption of other, larger molecules can be seen. It must be noted that for the molecules corresponding to fragmentation patterns of the parent ices, the main contribution to the signal is originating from the non irradiated part of the sample holder, as the data have not been corrected for the blank measurements. (For a color version, the reader is referred to the web version of this article.)

four (blue) hour experiments. The  $m/z = 28$  signal has been omitted in all experiments due to the prominent contribution of nitrogen in the nitrogen containing experiments. The third panel shows the difference between the two and four experiments for each mass. This makes it possible to assess how mass signatures of irradiation products evolve over the course of the experiment.

These figures allow us to identify molecules in the data and visualize differences and similarities between the experiments. In the following sections, identifications and trends of various groups of molecules will be discussed. In order to identify molecules based on their electron ionization fragmentation pattern, data from the NIST Chemistry WebBook (<http://webbook.nist.gov>) are used and fitted to the measured data.

### 3.1. Identification and trends of $C_2H_x$ species

The first sign of newly formed species during the irradiation can be seen between 70 and 80 K in the TPD, indicated in Fig. 4 with a red box. There, a number of coinciding desorption peaks for masses between  $m/z=24$  and 30 are detected. A detailed view of the desorption trace of selected  $m/z$  in this mass range is shown in Fig. 6. These signals most likely originate from small hydrocarbons, specifically  $C_2H_x$  species. The assignment of these desorption signals to  $C_2H_x$  species is further supported by the desorption temperature, which is in good accordance with previously measured desorption temperatures of small hydrocarbons (see Behmard et al., 2019).

The peak desorption temperature for the  $C_2H_x$  species varies for the different ices: For the  $CH_4:N_2$  2 and 4 h experiments the peak desorption temperature is located at  $T = 73 \pm 1$  K, whereas for the  $CH_4:H_2O$  and  $CH_4:H_2O:N_2$  2 h experiments the peak desorption

temperature is located at  $T = 81 \pm 1$  K. This difference in desorption temperatures between the ices most likely originates from the different binding environments introduced by amorphous water ice, which has been observed to shift desorption temperatures of small hydrocarbons to higher temperatures (Behmard et al., 2019).

The majority of the desorption signal assigned to  $C_2H_x$  disappears during the TPD of the 4 h irradiated  $CH_4:H_2O$  and  $CH_4:H_2O:N_2$  ices, as seen in the absence of corresponding desorption peaks in Fig. 4. The detailed view in Fig. 6 shows only a small peak for  $CH_4:H_2O$  4 h irradiation at 80 K, whereas the peak completely disappears for the  $CH_4:H_2O:N_2$  4 h irradiation. For the  $CH_4:N_2$  ices, desorption peaks assigned to  $C_2H_x$  appear in both the 2 and 4 h irradiation with no clear decrease in signal strength for the 4 h irradiation. This suggests that the hydrocarbons might not be destroyed during the 4 h irradiation of the  $CH_4:H_2O:N_2$  and  $CH_4:H_2O$  ices, but instead are incorporated into more complex molecules. The presence of water and the formation of radiolysis products like the hydroxyl radical (OH) could play a role in the quicker consumption of the small  $C_2H_x$  species.

Fig. 7 shows the data of the desorption peak at  $T \sim 80$  K for the 2 h irradiated ices, which have been fitted with NIST fragmentation patterns of the  $C_2H_x$  species. The ratios of the contributions are normalized to ethane and shown in Table 3. The fit suggests that ethane is the main contribution to this desorption signal for all three ices, which is in accordance with findings in other studies on irradiated methane, such as Bennett et al. (2006). Furthermore, all three ices show a similar relative contribution of ethylene. However, acetylene is a minor contribution to the desorption signal for both  $CH_4:H_2O:N_2$  and  $CH_4:N_2$ , whereas it is still a major contribution for  $CH_4:H_2O$ . This either indicates that  $C_2H_6$  and  $C_2H_4$  are not readily formed or easily

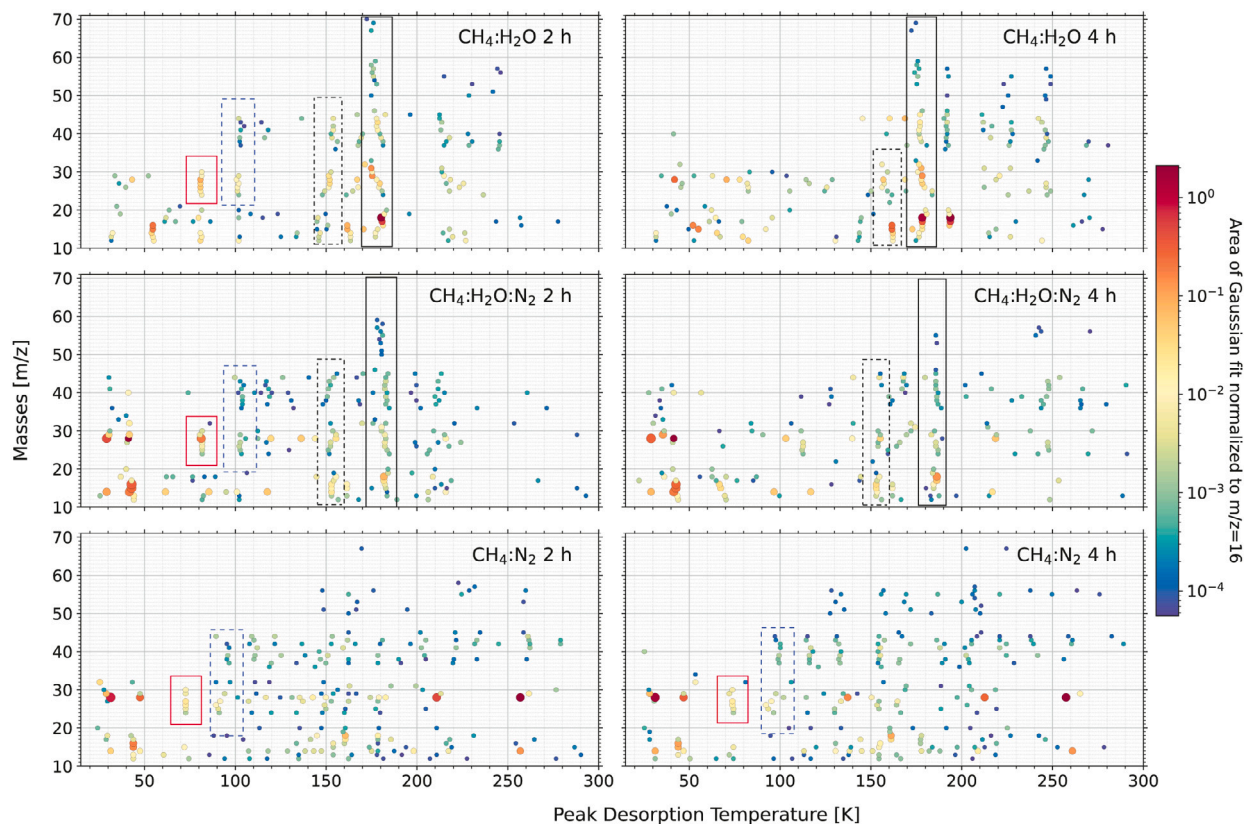


**Fig. 4.** Peak desorption temperatures of desorption events from the irradiated ices. The data used in this plot have been corrected for the blank measurements. The masses  $m/z < 10$  have been omitted, as no prominent irradiation products besides  $m/z = 2$  ( $\text{H}_2$ ) have been detected for this mass range. To quantify the peaks, each peak detected has been fitted with a Gaussian function centered at the peak location. For each measurement, the area of the Gaussian fit has been normalized to the highest value detected for  $m/z = 16$  over all measurements to allow direct comparison. Only peak areas with a normalized area larger than  $5 \cdot 10^{-5}$  compared to the highest  $m/z = 16$  signal over all measurements, assumed to belong to  $\text{CH}_4$ , have been taken into account. The color and size of the data points correspond to the area of this Gaussian fit, with bigger size of the data points corresponding to a bigger area. Different regions of interest have been indicated, such as the  $\text{C}_2\text{H}_x$  desorption (red, solid box), the  $\text{C}_3\text{H}_x/\text{C}_2\text{H}_x$  desorption (blue, dashed box), the phase change of water ice from amorphous to cubic (black, dashdot box), and the desorption of water (black, solid box). (For interpretation of the references to color in this figure legend, the reader is referred to the web version of this article.)

consumed, potentially to form  $\text{C}_2\text{H}_2$ , in the  $\text{H}_2\text{O}:\text{CH}_4$  mixture or that  $\text{N}_2$  or its radiolysis products react with  $\text{C}_2\text{H}_2$ , therefore lowering its abundance. The  $m/z = 24$  and  $m/z = 25$  are consistently underfitted for all three ices. However, contributions from pure  $\text{C}_2$  and  $\text{C}_2\text{H}$  from the ice are unlikely because they are radicals and would have likely reacted in the ice during or before the TPD. Therefore, the underfitting rather points to a difference in the electron ionization fragmentation pattern between species in the NIST database and the measurement of the molecules with the ICEBEAR setup.

A second desorption of  $\text{C}_2\text{H}_x$  is observed at 100 K for the  $\text{CH}_4:\text{H}_2\text{O}$  and  $\text{CH}_4:\text{H}_2\text{O}:\text{N}_2$  2 h experiments, though the desorption signal is reduced compared to the first desorption event at 80 K. For both  $\text{CH}_4:\text{N}_2$  experiments, desorption peaks are observed at  $T \sim 90$  K, again at a lower temperature compared to the ices containing water. Such a double peak structure has been observed for  $\text{C}_2\text{H}_2$  in the work by Collings et al. (2004), where  $\text{C}_2\text{H}_2$  has been deposited on top of water ice. This could point to the upper layer of the ice being processed during the irradiation and subsequently the formed  $\text{C}_2\text{H}_x$  is desorbing, therefore resulting in similar desorption characteristics as the ice shown in Collings et al. (2004). Furthermore, for  $\text{CH}_4:\text{H}_2\text{O}:\text{N}_2$  and  $\text{CH}_4:\text{H}_2\text{O}$ , two additional desorption peaks for the masses corresponding to  $\text{C}_2\text{H}_x$  are observed at  $T = 150$  K and  $T = 180$  K, during the desorption of water. These 100 K and co-desorption peaks will be discussed in more detail in Sections 3.2 and 3.3.

In Fig. 5, the 2 h experiments of all three ices show a similar trend for  $\text{C}_2\text{H}_x$  between 60 to 130 K, with the integrated signals for  $m/z = 26$  ( $\text{C}_2\text{H}_2^+$ ) and  $m/z = 27$  ( $\text{C}_2\text{H}_3^+$ ) being higher than those for  $m/z = 24$  ( $\text{C}_2^+$ ) and  $m/z = 25$  ( $\text{C}_2\text{H}^+$ ). The addition of nitrogen

**Table 3**

The prefactors used for  $\text{C}_2\text{H}_x$ ,  $\text{C}_3\text{H}_x$  and other irradiation products to reproduce the observed signal strength of the desorption peaks at  $T = 80$  K and  $T = 100$  K respectively for the 2 h irradiated ices. The fits can be seen in Figs. 7 and 9 and the values in this table have been normalized to the prefactor of ethane (80 K) and the prefactor of propane (100 K) respectively in order to compare the different experiments to each other. The prefactors have been determined by varying the values manually to best reproduce the observed pattern and are expected to represent a minimal amount of product. As no clear desorption peak is observed for  $\text{CH}_4:\text{N}_2$  at 100 K, the fit has also been performed for the continuous desorption denoted by Plateau in the Table.

	$\text{CH}_4:\text{H}_2\text{O}$	$\text{CH}_4:\text{H}_2\text{O}:\text{N}_2$	$\text{CH}_4:\text{N}_2$	
				80 K
Ethane	1.00	1.00	1.00	
Ethylene	0.88	0.79	0.69	
Acetylene	0.47	0.13	0.08	
				100 K
Ethane	1.00	0.00	0.47	0.12
Ethylene	9.10	0.14	0.47	0.08
Acetylene	5.50	2.22	2.67	0.33
Hydrogen Cyanide	0.00	2.11	2.33	0.33
Propane	1.00	1.00	1.00	1.00
Cyclopropane	0.10	0.00	0.00	0.08
Propene	0.00	0.03	0.00	0.00
Carbon Dioxide	3.20	2.57	0.00	0.00
Ketene	0.00	0.05	0.00	0.00
Formaldehyde	0.00	0.27	0.00	0.00
Cyclopropene	1.25	0.54	0.23	0.08

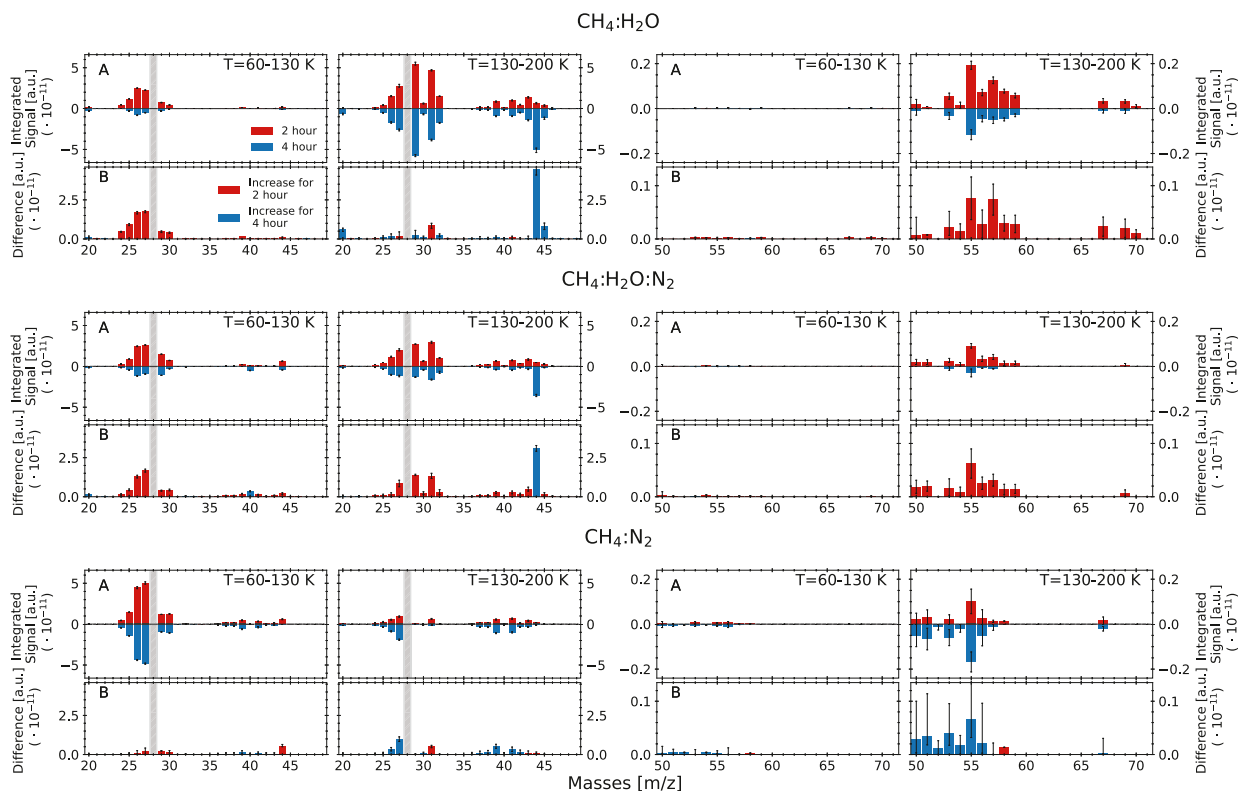


**Fig. 5.** A: The integrated desorption trace for the 2 h (red) and 4 h (blue) irradiation during the indicated temperature regime. The 4 h signal has been plotted on a negative axis for clarity. The data have been corrected for the blank measurement. The error has been determined by analyzing the root mean square between the raw and filtered data and subsequently using the ratio between the root mean square and the highest peak.

B: The difference between the 2 and 4 h irradiation, a red bar is shown, if more signal is detected for the 2 h irradiation, a blue bar.

The left columns show the masses  $m/z = 20$  to  $m/z = 49$ , the right columns  $m/z = 50$  to  $m/z = 71$ . For higher  $m/z$ , there were no desorption signals that could be confidently distinguished from noise, for lower  $m/z$ , the signal is dominated by the  $m/z$  signals from the parent ices and no clear irradiation products were identified. The columns are plotted on different scales to highlight the lower signals of the higher masses. Two different temperature regimes are investigated,  $T = 60\text{--}130$  K, where volatile complex molecules desorb, and  $T = 130\text{--}200$  K, which covers the water desorption regime (if applicable). After the water desorption, only isolated signal for the majority of the  $m/z$  is detected, therefore this temperature regime is omitted. The measurement for  $m/z = 28$  has been excluded due to the strong influence of the nitrogen signal, even after subtracting the blank. For homogeneity of the figure, the measurement is also excluded for the  $\text{CH}_4:\text{H}_2\text{O}$  ice. (For interpretation of the references to color in this figure legend, the reader is referred to the web version of this article.)

to the  $\text{CH}_4:\text{H}_2\text{O}$  mixture does not appear to influence the signal of  $\text{C}_2\text{H}_x$  in this temperature regime significantly, with the relative signal strength remaining similar for the two ices. However, as mentioned in the previous paragraphs, a significant decrease in the signal of  $\text{C}_2\text{H}_x$  between the 2 h irradiation and the 4 h irradiation is observed for both ices containing water. For  $\text{CH}_4:\text{N}_2$ , the difference between the signal of the 2 and 4 h irradiation is negligible. As the  $\text{CH}_4:\text{N}_2$  ice contains the highest total amount of methane of all ices, the increased signal observed for this ice for  $m/z = 26$  and  $m/z = 27$  indicates that the signal indeed originates from  $\text{C}_3\text{H}_x$ , in this case most likely from acetylene ( $\text{C}_2\text{H}_2$ ) and ethylene ( $\text{C}_2\text{H}_4$ ). As the signal for  $m/z = 28$  ( $\text{C}_2\text{H}_4$ ) was excluded, no comparative information can be derived for the different ices. However, the strong  $m/z = 27$  signal in all ices points to the presence of  $\text{C}_2\text{H}_4$  with  $m/z = 27$  being part of the fragmentation pattern. The fit derived in Fig. 7 supports this hypothesis.

### 3.2. Identification and trends of $\text{C}_3\text{H}_x$ species

Coinciding desorption peaks of masses  $m/z = 36$  to  $43$ , as well as  $m/z = 24$  and  $30$  are observed between  $90$  and  $100$  K, see the blue, dashed box in Fig. 4. A closeup of selected  $m/z$  in this mass range is shown in Fig. 8, showing the desorption trace.

The higher masses could be related to the release of small hydrocarbons consisting of  $\text{C}_3\text{H}_x$  species.  $\text{C}_3\text{H}_x$  are common irradiation products in carbon rich ices and can be produced from the irradiation

of  $\text{C}_2\text{H}_x$  (e.g. Hudson et al., 2009). While the  $\text{C}_3\text{H}_x$  molecules have fragmentation patterns that show up at  $m/z = 24\text{--}30$ , their contribution to this mass range is minor, see Fig. 3. The desorption temperature observed in this work of  $\text{C}_3\text{H}_x$  species matches the temperatures recorded in previous work by Behmard et al. (2019).

Similar to  $\text{C}_2\text{H}_x$  as discussed in Section 3.1, a slight shift in the position of the desorption peaks for the  $\text{CH}_4:\text{H}_2\text{O}$  and  $\text{CH}_4:\text{H}_2\text{O}:\text{N}_2$  ices compared to the  $\text{CH}_4:\text{N}_2$  ice is observed for the  $\text{C}_3\text{H}_x$  species. For the ices containing water, the desorption peak is located at  $102 \pm 1$  K, while for  $\text{CH}_4:\text{N}_2$  it is found at  $96 \pm 1$  K. However, as seen in Fig. 8, for the  $\text{CH}_4:\text{N}_2$  ices a continuous desorption starting from  $90$  K of  $m/z$  assigned to  $\text{C}_3\text{H}_x$  species is observed rather than a sharp desorption peak. This could indicate desorption from a complex surface, which introduces a range of binding sites, likely leading to this desorption trace (see Corazzi et al., 2021, for an example of this effect on desorption from olivine grains).

Fig. 4 shows that the desorption peaks assigned to  $\text{C}_3\text{H}_x$  are observed for the 2 h irradiated ice in the case of  $\text{CH}_4:\text{H}_2\text{O}$  and  $\text{CH}_4:\text{H}_2\text{O}:\text{N}_2$ , but, analog to previous observation of  $\text{C}_2\text{H}_x$ , disappear for the respective 4 h experiment. For  $\text{CH}_4:\text{N}_2$ ,  $\text{C}_3\text{H}_x$  desorption signals are detected in both the 2 and 4 h irradiated ices, with the difference in integrated signal between the irradiation times negligible, see Fig. 5.  $\text{C}_3\text{H}_x$  signal is also detected for  $\text{CH}_4:\text{H}_2\text{O}$  and  $\text{CH}_4:\text{H}_2\text{O}:\text{N}_2$ , though at smaller intensity than for  $\text{CH}_4:\text{N}_2$ . Furthermore, Fig. 8 shows that for the ices containing water, the main desorption event of  $\text{C}_3\text{H}_x$  species

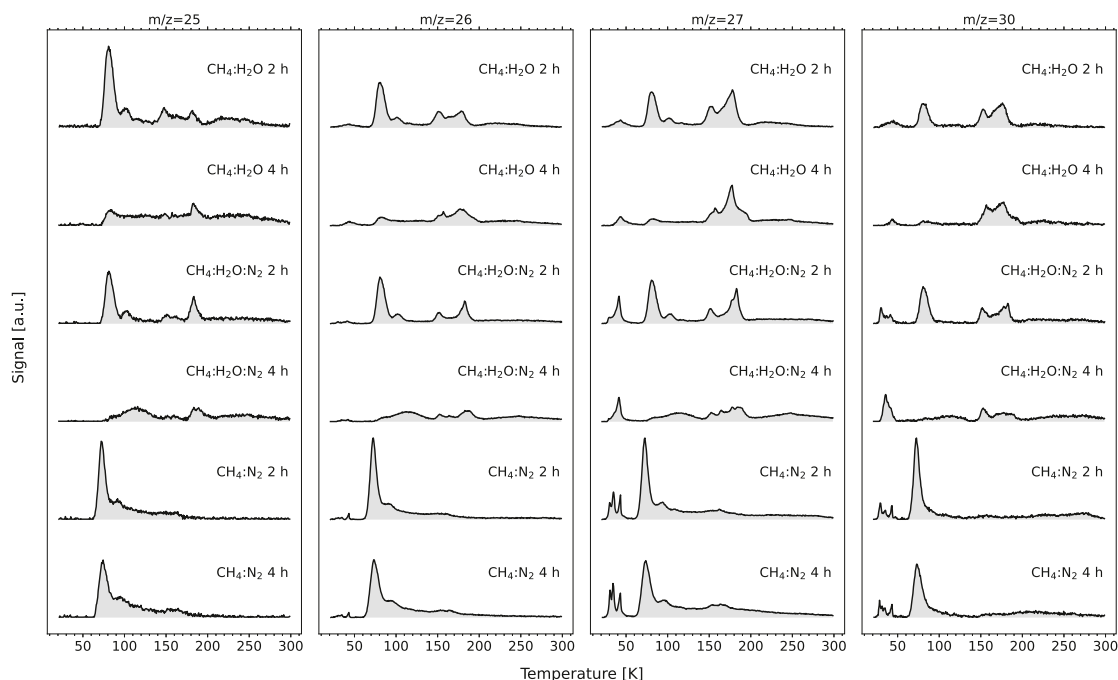


**Fig. 6.** TPD data collected for the irradiated ices. In these panels, desorption traces of  $m/z = 25, 26, 27,$  and  $30$  are shown, which are presumed to be signals largely corresponding to parents and fragments of  $C_2H_x$ . Fragments from larger molecules and directly produced smaller hydrocarbons themselves are expected to contribute to the signal. Blank measurements have been collected, but show no significant peaks for the presented masses, indicating that these signals originate from molecules produced during the electron irradiation. All measurements shown in one panel are plotted on the same scale and the curves have been offset from each other. The area under the curve has been shaded to better show the presence of low signal.  $m/z=28$  and  $m/z=29$  have not been included in this figure due to the strong contribution of the  $N_2$  peak for the experiments containing nitrogen, see Fig. B.15 in the Appendix A.

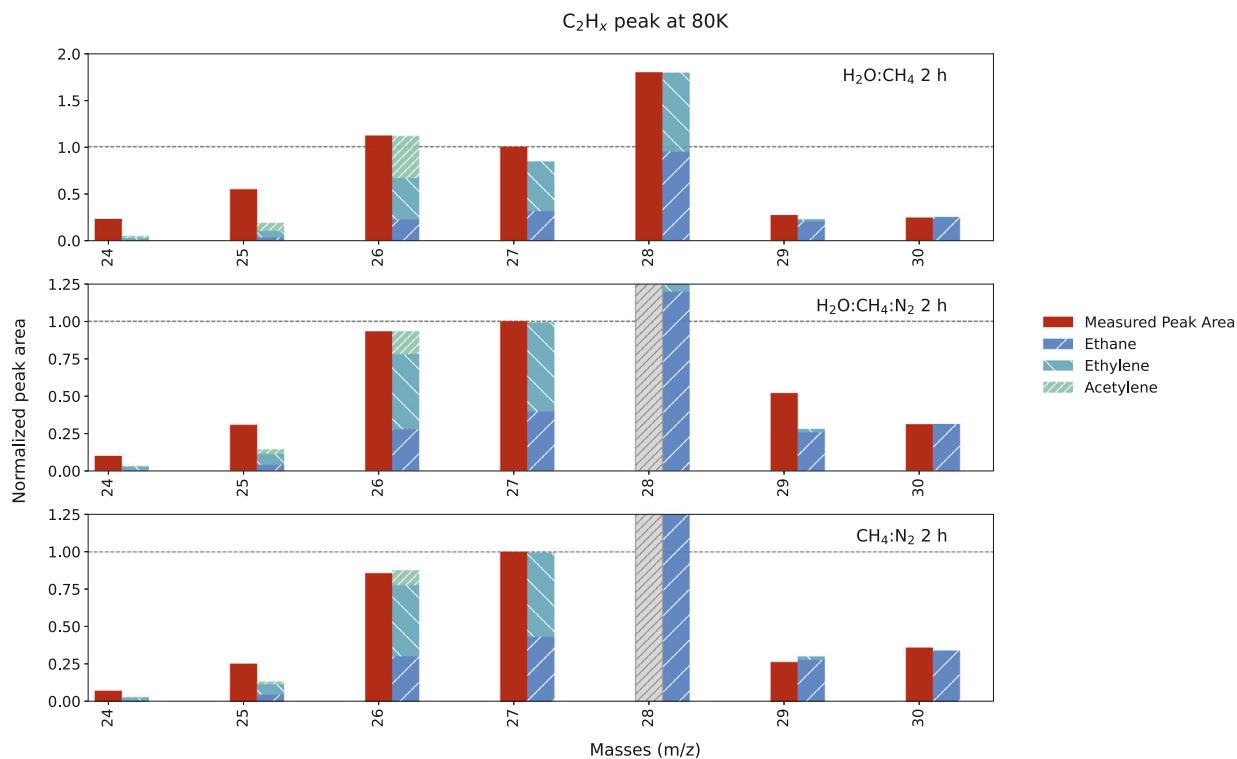


**Fig. 7.** Fitting of the peak area of multiple  $m/z$  with a peak desorption around  $T = 80$  K for the 2 h irradiated ices with the electron ionization mass spectrum of different  $C_2H_x$ . The measured data have been fitted with a Gaussian function, centered at the temperature of the desorption peak. Contributions from other molecules to a  $m/z$ , such as for example  $N_2H_2$ , could not be excluded, but no data are available for these molecules in the NIST database.  $m/z = 28$  has been omitted from the nitrogen containing experiments due to the strong influence of  $N_2$  at this temperature, which does not allow peak detection. The areas of the Gaussian fits have been normalized to  $m/z = 27$  in all cases. The dashed line indicates the normalization to  $m/z = 27$ .

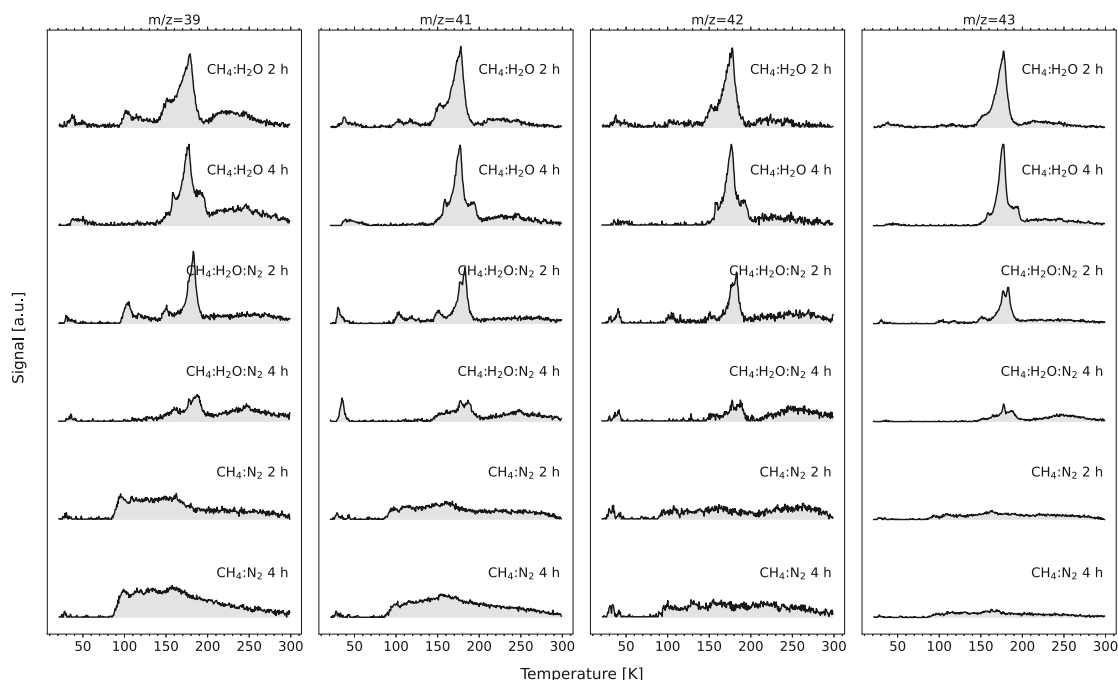


**Fig. 8.** TPD data collected for the irradiated ices. In these panels,  $m/z = 39, 41, 42,$  and  $43$  are shown, which are presumed to be signals corresponding to  $C_3H_x$ . Fragments from larger molecules themselves are assumed to contribute to the signals as well. All measurements shown in one panel are plotted on the same scale and the curves have been offset from each other, but the scale differs from panel to panel. The area under the curve has been shaded in order to better show the presence of relatively low signal.

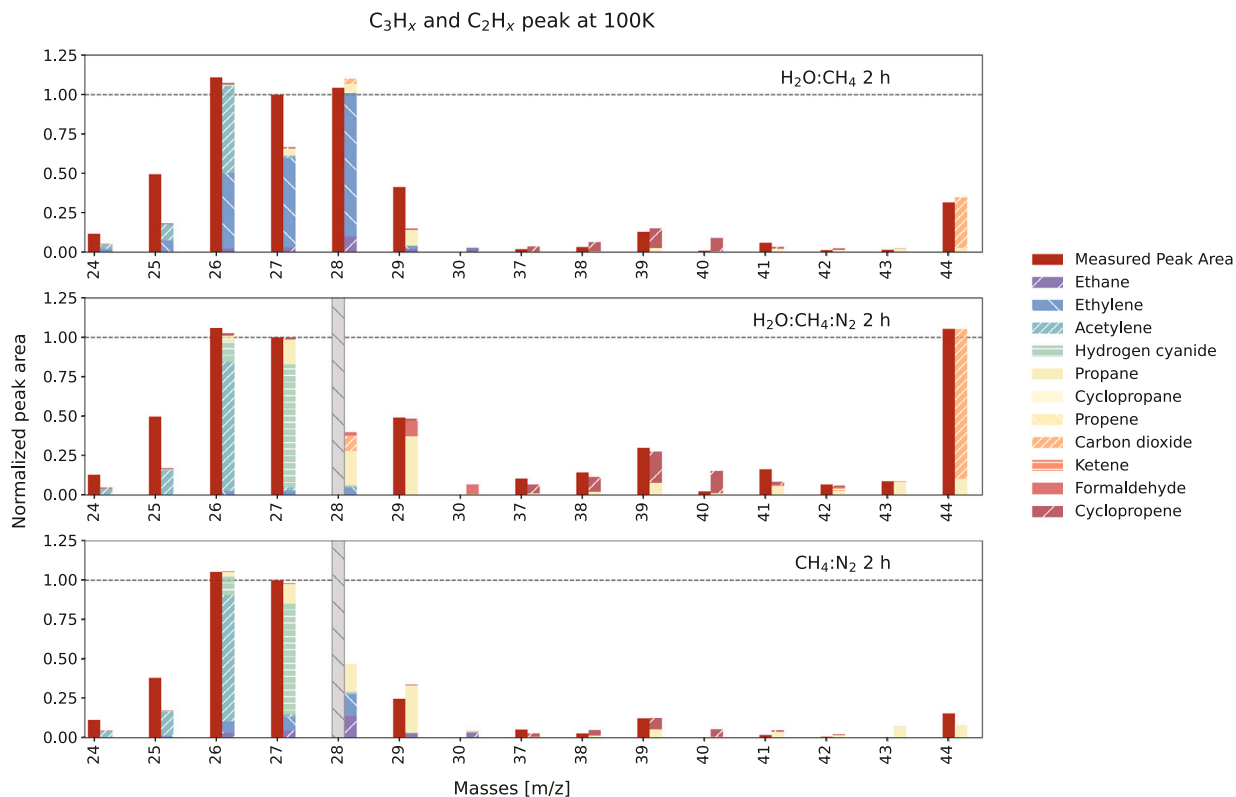


**Fig. 9.** Fitting of the peak area of multiple  $m/z$  at  $T = 100$  K for the 2 h irradiated ices with the electron ionization mass spectrum of  $C_2H_x$ ,  $C_3H_x$  and selected other molecules, such as  $CO_2$ . The measured data have been fitted with a gaussian function, centered at the temperature of the desorption peak. A manual fit has been performed in order to estimate the contributions of the different molecules to the total signal. Note that  $m/z = 28$  has been excluded from the nitrogen containing ices, due to a large contribution of continuous desorption of  $N_2$ . Contributions from other molecules, such as  $N_2H_2$  to  $m/z = 29$  could not be excluded, but no data are available for these molecules in the NIST database. The legend lists the molecules that have been considered for this fit.

occurs at around  $T \sim 180$  K, which will be discussed in more detail in Section 3.3.

An attempt has been made to fit the fragmentation pattern of various  $C_3H_x$  and  $C_2H_x$  species to the observed signal, the result of which can be seen in Fig. 9. The fit ratios are presented in Table 3. Based on the fit, propane ( $C_3H_8$ ) and cyclopropene ( $C_3H_4$ ) are suggested to be the main  $C_3H_x$  species that contribute to the desorption signal at this temperature, although we note that the expected cyclopropene fragment at  $m/z = 40$  is largely missing from the data. Notably, the prominent contribution of ethane to  $m/z=30$  in the  $\sim 80$  K desorption event is now largely absent for all three ices at this desorption temperature. This suggests that for all three ices the majority of ethane is desorbing during the first  $C_2H_x$  desorption event, whereas acetylene and ethylene are at least partially co-desorbing with  $C_3H_x$  at  $T \sim 100$  K (Behmard et al., 2019). Furthermore, for  $CH_4:H_2O$  and  $CH_4:H_2O:N_2$ ,  $CO_2$  desorption is likely to occur at this temperature based on the prominent  $m/z = 44$  signal. The desorption temperature of 90–100 K is in reasonable accordance with the peak desorption temperature derived by Collings et al. (2004), which is just above 80 K for  $CO_2$  adsorbed on water ice.

Finally, to properly fit the  $m/z = 26$  and 27 pattern of  $CH_4:H_2O:N_2$  and  $CH_4:N_2$  a contribution of hydrogen cyanide (HCN) is included. Experiments by Bergner et al. (2022) on HCN desorption show that this molecule desorbs around 110–120 K for multilayer HCN or monolayer HCN on top of  $H_2O$  desorption, which is in reasonable agreement with the temperature of the desorption event investigated here. A substantial amount of HCN is produced in the  $N_2$ -doped ices (see Table 3), but we note that due to the poor constraints on the  $m/z = 28$  signal caused by the continuous presence of molecular nitrogen, there is some uncertainty to the ethylene fit, which can result in an overestimation of the HCN contribution. Presumably, a large portion of produced HCN desorbs around 180 K, see Fig. 6.

### 3.3. Trends during volcano and co-desorption

Figs. 3 and 4 show two prominent desorption events for the  $CH_4:H_2O$  and  $CH_4:H_2O:N_2$  ices, with peak desorption temperatures at  $T \sim 150$  K and  $T \sim 180$  K. The first desorption event at 150 K can be attributed to the desorption of molecules due to the phase change of water from amorphous to cubic, allowing previously trapped molecules to escape. This effect is often referred to as volcano desorption (Bar-Nun et al., 1985) and marked by a dash-dotted black box in Fig. 4. The second desorption at 180 K corresponds to the water desorption, with which the remaining molecules can co-desorb (Bar-Nun et al., 1985; Collings et al., 2004). It is indicated by a dashed black box. Both the volcano and co-desorption of molecules are linked to the presence of water in the ice and therefore no such localized desorption is observed for the experiments making use of the  $CH_4:N_2$  ices. Instead, a continuous desorption trace is observed for larger  $m/z$ , as has already been discussed in Section 3.2.

A number of observations can be made: First, the species released with water follow a pattern. For the volcano desorption, ions are detected at  $m/z = 24$ –30 and 37–44, while for the co-desorption event masses at  $m/z = 24$ –32,  $m/z = 37$ –44, and  $m/z = 52$ –59 are identified. In the case of the  $H_2O:CH_4$  irradiation experiment, species at  $m/z = 69$  are also found. Contributors to these desorption events are expected to be hydrocarbons following the  $C_2H_x$ ,  $C_3H_x$ ,  $C_4H_x$  pattern, but oxygen-bearing molecules with elemental compositions of  $COH_x$ ,  $C_2OH_x$ , and  $C_3OH_x$  could also contribute. Methanol ( $CH_3OH$ ) is likely part of the species co-desorbing with water, because the intensity of the measured ions at  $m/z = 31$  and 32 match well with the NIST fragmentation pattern of methanol. However, other fragments (e.g.,  $m/z = 28$ , 29) cannot be fitted due to contributions to these  $m/z$  signals of other species. Tentative evidence for a larger alcohol is seen in Fig. 5, where for  $CH_4:H_2O$  and  $CH_4:H_2O:N_2$  an increase in  $m/z = 57$ , 58, and 59 is seen, not observed for  $CH_4:N_2$ . This suggests that not only a pattern of small hydrocarbons can be seen, but also of alcohols.

Second, the volcano and co-desorption signal intensities decrease from the 2 h to the 4 h experiment. In the case of the  $CH_4:H_2O:N_2$ , signal indicating the desorption of larger molecules ( $m/z \geq 50$ ) are absent in the 4 h irradiation experiment. This difference is exemplified in Fig. 5 in the  $T = 130$ –200 K panel. Only the signal of  $m/z = 44$  increases from 2 h to 4 h irradiation, whereas all the others decrease. The continued irradiation of the products likely results in the formation of more complex and non-volatile species or the formation of  $CO_2$  from oxygen atoms and hydroxyl radicals (OH) reacting with organic molecules. The latter event explains the increased presence of  $CO_2$ .

### 3.4. Desorption versus co-desorption

The presence of water has been shown to influence the desorption behavior of the irradiation products, with co-desorption being the main desorption event in the case of  $CH_4:H_2O$  and  $CH_4:H_2O:N_2$ , whereas a continuous desorption is dominant for most species in the case of  $CH_4:N_2$ . To compare the overall desorption trends and identify similarities or differences, the total desorption signal of selected  $m/z$  has been integrated from 60 to 300 K, the result for which is shown in Fig. 10.

Taking into account that  $CH_4:N_2$  has a higher abundance of  $CH_4$  than  $CH_4:H_2O$  or  $CH_4:H_2O:N_2$ , the integrated signal over the whole temperature range for  $C_3H_x$  species ( $m/z = 36$ –42) is similar for all three ices. Therefore the total amount of  $C_3H_x$  produced during the irradiation seems to be comparable for the three ices, but the majority of  $C_3H_x$  co-desorbs with water for the  $CH_4:H_2O$  and  $CH_4:H_2O:N_2$  mixtures, see Fig. 8.

The picture for  $m/z = 24$ –32 is more complex. Fig. 10 shows a decrease in the  $C_2H_x$  signal from the 2 to the 4 h irradiation for both  $CH_4:H_2O$  and  $CH_4:H_2O:N_2$ , as well as a general decrease in signal in  $CH_4:H_2O:N_2$  compared to  $CH_4:H_2O$ . This is further evidence that simple  $C_2H_x$  products are consumed with prolonged irradiation, but also that the addition of nitrogen to the ice mixture leads to lower abundances of volatile molecules and presumably the incorporation into a refractory residue. For  $CH_4:N_2$ , the opposite effect is observed for the majority of  $m/z$ , with the 4 h irradiation resulting in an increase of the total desorption signal, which could indicate that water is needed to form a residue that effectively incorporates molecules.

As discussed in Sections 3.1 and 3.2, the desorption behavior of smaller hydrocarbons after 2 h of irradiation for  $CH_4:H_2O$  and  $CH_4:H_2O:N_2$  is in accordance with desorption of molecules deposited on top of a water ice layer. For the 4 h irradiation however, the desorption behavior is more in accordance with TPD spectra of co-deposited ices, see Collings et al. (2004). This suggests that for a longer irradiation duration, the desorbing species are incorporated more efficiently into the water matrix.

The signal for  $m/z = 29$ , 31, and 32 observed for  $CH_4:H_2O$  and  $CH_4:H_2O:N_2$ , as well as the significant decrease in case of the  $CH_4:N_2$  ice, support the assignment of these  $m/z$  to the formation of methanol, with the addition of nitrogen to  $CH_4:H_2O$  again leading to a decrease in total desorption signal. The presence of methanol suggests that it could get processed further, leading to the formation of larger alcohols. However, no unambiguous evidence for these larger alcohols has been seen in the data, though the trend for  $m/z = 55$ , 57, 58, and 59 for  $CH_4:H_2O$  and  $CH_4:H_2O:N_2$  not observed for  $CH_4:N_2$  suggests their presence.

Apart from tentative identification of HCN or HNC, only very small signals for molecules formed exclusively in the irradiation of  $CH_4:N_2$  ices could be distinguished in the present study. Based on the data in Fig. 10, where an increase for  $m/z = 30$  can be observed for both irradiation times of  $CH_4:H_2O:N_2$ , compared to the respective measurement of  $CH_4:H_2O$ , the signal at  $m/z=30$  is tentatively assigned to  $N_2H_2$ . Kim and Kaiser (2012) have observed the formation of various nitrogen bearing molecules upon the irradiation of  $N_2:CH_4:CO$  ices. However, their findings are based on spectroscopic data, therefore the molecules could still be formed in the present study, but remain trapped in the

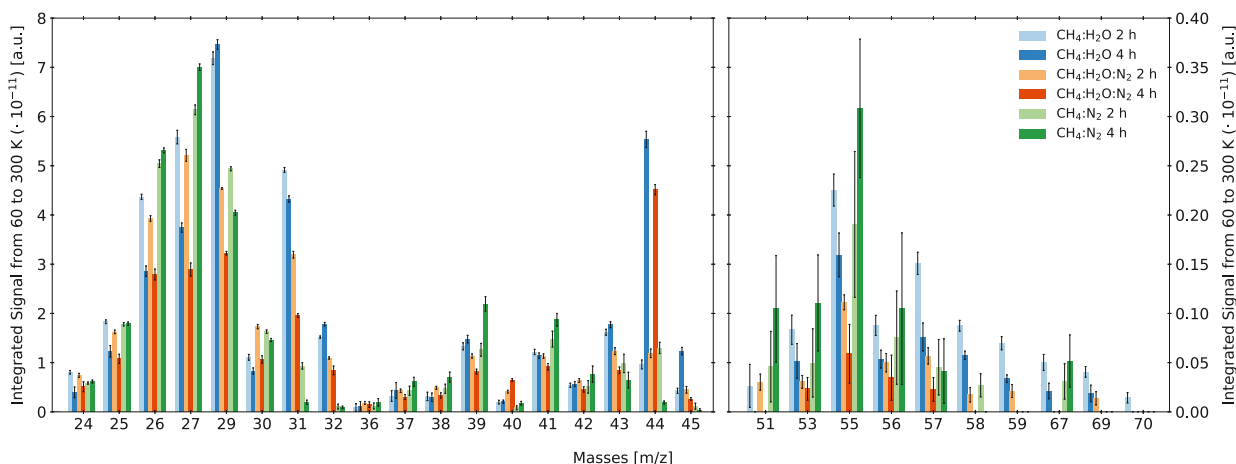


Fig. 10. Integrated Signal from 60 K to 300 K. For the  $m/z > 50$ , a different scale has been implemented in order to highlight the low signals. Only masses for which a clear peak detection has been possible and with relevance to the species discussed in previous sections are included.



Fig. 11. Evolution of an  $\text{CH}_4\text{:H}_2\text{O:N}_2$  ice that has been irradiated for 4 h during the TPD. The desorption of various molecules can be clearly seen in the color change on the sample holder. A brownish residue remained on the sample holder after the TPD was completed. (For interpretation of the references to color in this figure legend, the reader is referred to the web version of this article.)

residue, and are therefore not detected during the TPD with the QMS. A TPD has been performed in the study by Kim and Kaiser (2012), but the data are not shown, therefore no comparison can be made to the results in the present study.

### 3.5. Formation organic residues

An example of the evolution of the products formed during irradiation is shown in Fig. 11, where the  $\text{CH}_4\text{:H}_2\text{O:N}_2$  ice is shown after 4 h of irradiation at 20 K, corresponding to experiment III in Table 1. The residue is shown at various temperature intervals ranging from 20 to 300 K. Other experiments show a similar progression and the particular example is used to illustrate the change in the sample appearance over the course of the TPD, including changes related to the ice composition.

At the beginning of the TPD (top left), the darkened irradiated area can be seen, indicating that chemical reactions have taken place during

the irradiation, leading to the color change. From 20 to  $\sim 40$  K, the irradiated area shows a higher contrast to the surrounding area. At  $\sim 45$  K,  $\text{CH}_4$  and  $\text{N}_2$  have desorbed from the sample holder surface and this change is apparent for the image at 46.75 K, in which the irradiated area shows an even higher contrast to the pristine ice on the sample holder. Afterwards, the irradiated area slightly changes color, until  $\sim 150$  K, at which a second, albeit smaller methane desorption is observed due to volcano desorption with water (see the corresponding experiment in panel  $m/z = 16$  for Fig. B.15 in the Appendix A). Afterwards, the water desorption begins, which has its peak desorption at roughly  $\sim 175$  K. This can also be seen in the images, as the sample holder around the irradiated spot returns to the initial coloration with the water gone. After the water desorption, further color changes can be observed for the irradiated area, as well as the evolution of smaller spots, where material is assumed to further desorb from the irradiated area. The onset of this spot formation is already seen at 40 K but extensive formation is only observed after the water desorption. This suggests that chemical processes are still ongoing in the residue, even after the water has desorbed.

After reaching 300 K, the residue remained on the sample holder surface until the chamber was opened, allowing for a closer inspection of the residue. The residue was observed to not dissolve when water was added, but could be dissolved with Isopropanol or Ethyl Acetate. A supplementary experiment performed on  $\text{H}_2\text{O:N}_2$  (not shown) did not result in residue formation. For all other irradiated ice mixtures discussed in this study and both irradiation times a residue was observed. However the residue visually appeared different depending on the ice irradiated: The least surface coverage of residue was observed for the  $\text{CH}_4\text{:N}_2$  residue, more surface coverage for the  $\text{CH}_4\text{:H}_2\text{O}$  ices and the most surface coverage for the irradiated  $\text{CH}_4\text{:H}_2\text{O:N}_2$  ice, which could correlate with the decrease in desorption signal. Therefore, the addition of nitrogen to the  $\text{CH}_4\text{:H}_2\text{O}$  ice is suggested to decrease the amount of volatile molecules formed during irradiation and locks up more material in a solid organic residue. In order to investigate this hypothesis, further analysis of the residues is necessary and will be the subject of future work.

## 4. Astrophysical implications

The mixed ices consisting of water, methane, and nitrogen are of relevance for objects in the outer solar system. There, planetary objects can have surfaces that are dominated by nitrogen or methane ice, such as Pluto Owen et al. (1993) or Makemake (Perna et al., 2016). Although

their surface is dominated by water ice, comets contain other ice components, among them nitrogen (Rubin et al., 2019) and methane (Gibb et al., 2003). The mixtures presented in this work therefore represent chemical extremes on either a KBO or a comet, which get processed via electrons. Even though the ices chosen in this work are relatively thin compared to the thickness of the ice sheets on comets or KBO, the penetration depth of 5 keV electrons is in the order of  $\mu\text{m}$  into the ice and could therefore simulate the processing of the upper most ice layers by energetic electrons and secondary electrons.

The energetic processing of various ices containing simple organic molecules, such as  $\text{CH}_4$ , has been shown to lead to the formation of a residue with colors ranging from orange, brown, and red. These refractory residues are referred to as tholins and have been proposed to at least be partially responsible for the coloration of several planetary bodies in the outer solar system (Sagan and Khare, 1979; Wilson et al., 1994; Cooper et al., 2003; Cruikshank et al., 2005; Raut et al., 2022). Tholins occur on the surface of various KBOs, such as Pluto Grundy et al. (2016), Makemake (Brown et al., 2015), and Ceres (Combe et al., 2019). Furthermore, they are also present in comets, being detected on 67P by the Rosetta mission (Wright et al., 2015). Indeed, as seen in Fig. 11, the residue observed during this work showed a brownish coloration after the desorption of volatile species, a process which could also occur non thermally on KBOs. This red coloration of the tholins is presumed to originate from the presence of hydrocarbons and nitriles, making it likely that the present mixture resulted in a tholin-like residue. Based on the findings in this study, it is suggested that the addition of nitrogen to the mixture leads to a more effective formation of tholins.

## 5. Conclusion and outlook

In this study, ices of different composition were prepared ( $\text{CH}_4:\text{H}_2\text{O}$ ,  $\text{CH}_4:\text{H}_2\text{O}:\text{N}_2$ , and  $\text{CH}_4:\text{N}_2$ ), which serve as analogues of the chemical extremes found on various Solar System objects, such as KBOs and comets. Irradiation with energetic electrons was used to induce chemical reactions and form new chemical compounds in the ices. Temperature Programmed Desorption coupled to Quadrupole Mass Spectrometry was employed to identify the product and indicate differences between the physicochemical process taking place in these ice mixtures. The findings and conclusions are summarized below:

1. The main products identified in all irradiated ices are hydrocarbons ( $\text{C}_2\text{H}_x$  and  $\text{C}_3\text{H}_x$ ), with  $\text{CO}_2$  and  $\text{CH}_3\text{OH}$  being additional irradiation products for the ices containing water, HCN for the ices containing molecular nitrogen.
2.  $\text{CH}_4:\text{H}_2\text{O}$  and  $\text{CH}_4:\text{H}_2\text{O}:\text{N}_2$  ices show significant differences in the peak desorption temperatures of  $\text{C}_2\text{H}_x$  and  $\text{C}_3\text{H}_x$  species compared to the  $\text{CH}_4:\text{N}_2$  ice. For  $\text{CH}_4:\text{N}_2$ , continuous desorption is observed for a multitude of molecules, pointing to desorption from a complex residue, which introduces a variety of binding sites and binding energies to desorb from.
3. For  $\text{CH}_4:\text{H}_2\text{O}$  and  $\text{CH}_4:\text{H}_2\text{O}:\text{N}_2$ , prominent co-desorption of molecules such as  $\text{C}_2\text{H}_x$ ,  $\text{C}_3\text{H}_x$  and larger molecules with water is observed. This, combined with the previous point, shows that the presence of water can change both the desorption temperature and behavior significantly. This could have implications for comets, which contain a large amount of water and are heated as they approach the Sun. Therefore, especially for larger molecules at low abundances, the molecules are expected to co-desorb with water. For KBOs or other icy planetary surfaces, where the temperature is generally below the water desorption temperature, this could lead to an accumulation of complex organic molecules. However, other non-thermal desorption mechanisms could still bring these molecules to the gas-phase.
4. A longer irradiation duration did generally not result in the formation of new compounds or larger abundances of volatile molecules, with the exception of  $\text{CO}_2$ . Instead, already at a radiation dose of approximately  $50 \text{ eV molecule}^{-1}$ , volatile products were incorporated into more complex, non-volatile species.
5. The addition of nitrogen to the  $\text{CH}_4:\text{H}_2\text{O}$  mixture shows a very similar trend for the desorption peaks, though the signal strength decrease as soon as nitrogen is added. Therefore the addition of nitrogen to the  $\text{CH}_4:\text{H}_2\text{O}$  mixture is interpreted to lead to a more effective incorporation of material in an organic residue. This could have implications for the processing of ice on the surface of KBOs or comets, suggesting that there could be an anti-correlation between nitrogen abundance and the desorption of complex molecules from energetically processed ice.

The analysis of the volatile irradiation products has already offered valuable insight in how the composition of the ice and irradiation duration influence the processing of ice and the desorption behavior of the resulting products. In order to achieve a more complete picture of the products, the residue remaining after the irradiation is subject of future work to complement the volatile desorption data. Furthermore, as clear identification of volatile molecules using QMS data is non

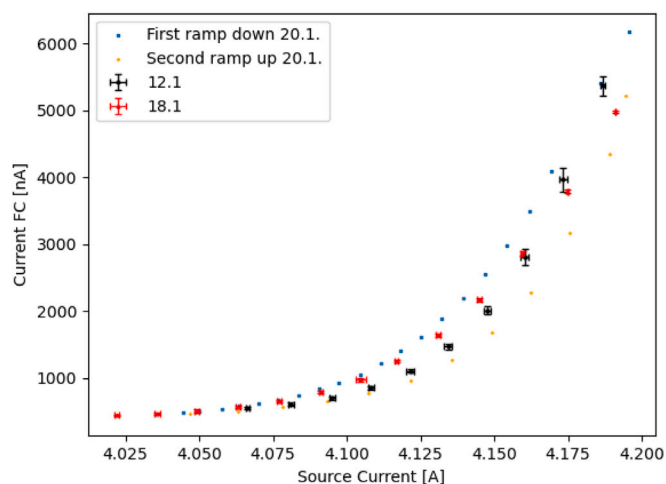


Fig. A.12. The measured current on the Faraday cup as a function of the source current applied to the Electron gun. Different measurements have been performed to see the relationship between the Source current and to investigate the stability. From these measurements, an error of around 10% was estimated for the current of the electron gun.

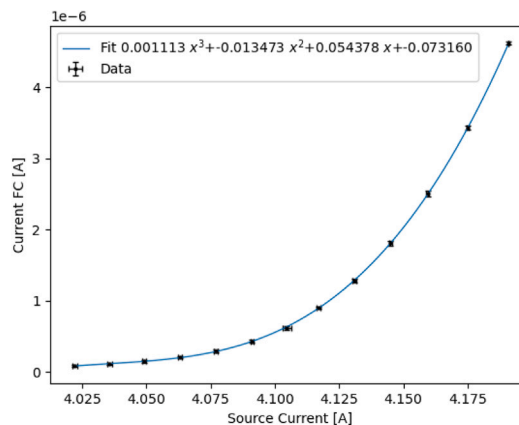


Fig. A.13. An average of the data that are shown in Fig. A.12, corrected for the background current. This plot was used to set the source current of the electron gun for all future experiments.

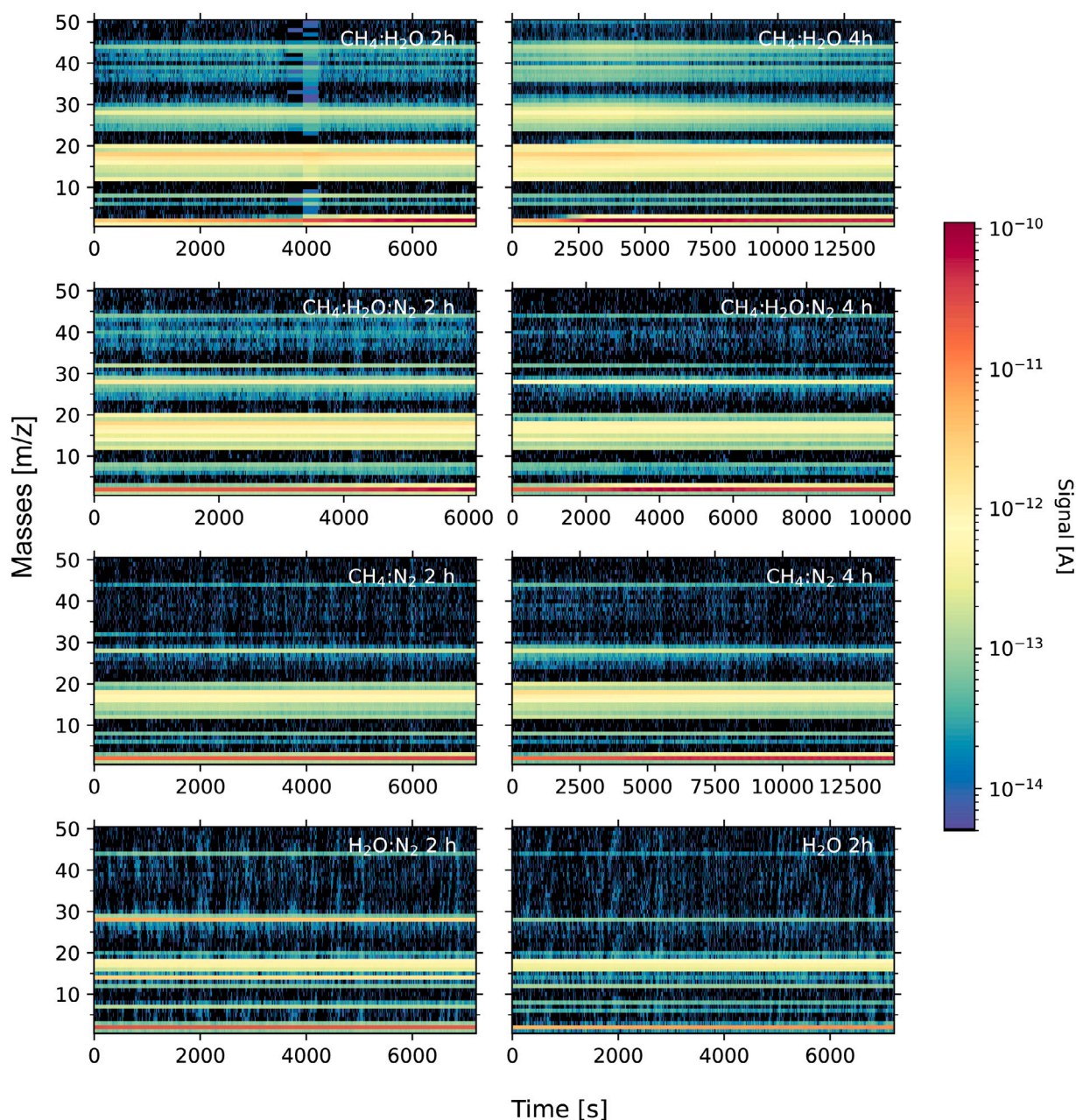


Fig. A.14. QMS data collected during the irradiation of the different ice samples. The irradiation of a pure  $\text{H}_2\text{O}$  ice has been included to show that there is negligible contribution from the electron gun to any  $\text{C}_2\text{H}_x$  or  $\text{C}_3\text{H}_x$  signals. Especially for  $\text{CH}_4:\text{H}_2\text{O}$ , non thermal desorption due to the irradiation can be seen, which appears to be much more effective in this case than the other ices. However, the signal is still comparatively weak compared to the  $\text{H}_2$  signal. For the  $\text{CH}_4:\text{H}_2\text{O}$  2 h irradiation, the interruption of the colorplot around 4000 s corresponds to an error with the QMS during the measurement. The same is true for both  $\text{CH}_4:\text{H}_2\text{O}:\text{N}_2$  2 and 4 h irradiation, where the last half hour is missing due to an error with the QMS.

trivial even for relatively simple ice mixtures, work is ongoing to implement an automatic molecule identification routine for TPD data analysis. Finally, the possible implications for the trapping of molecules in an organic residue will be investigated in future work with a special focus on the trapping of comparatively volatile molecules.

#### Declaration of competing interest

The authors declare that they have no known competing financial interests or personal relationships that could have appeared to influence the work reported in this paper.

#### Data availability

Data will be made available on request

#### Acknowledgments

K.A.K. and N.F.W.L. acknowledge support of the Swiss National Science Foundation (SNSF) Ambizione grant 193453. K.A.K., N.F.W.L. and A.R. acknowledge support from NCCR PlanetS. The authors want to thank the Space Research & Planetary Sciences fine mechanical and electronics departments, specifically: Raphael Hänggi, Sacha Häusler, Sébastien Hayoz, Iljadin Manurung, Harald Mischler, and Jan Wenger

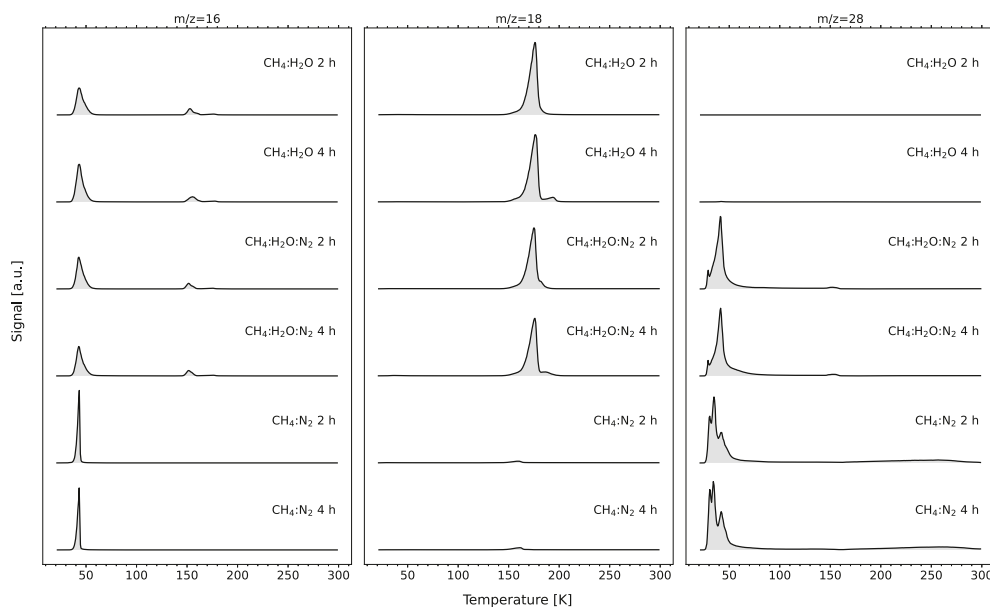


**Fig. B.15.** TPD spectra showing the evolution of the main mass signals for each experiment, with  $m/z = 16$  assumed to largely correspond to the signal of methane ( $\text{CH}_4$ ),  $m/z = 18$  to water ( $\text{H}_2\text{O}$ ), and  $m/z = 28$  to nitrogen ( $\text{N}_2$ ). The data have not been corrected for the blank measurement. All measurements shown in one panel are plotted on the same scale and the curves have been offset from each other, but the scales from panel to panel differ. Contributions to the signal of one  $m/z$  from different molecules cannot be excluded. The small peak for  $m/z = 18$  in the  $\text{CH}_4:\text{N}_2$  ices corresponds to residual water vapor in the chamber.

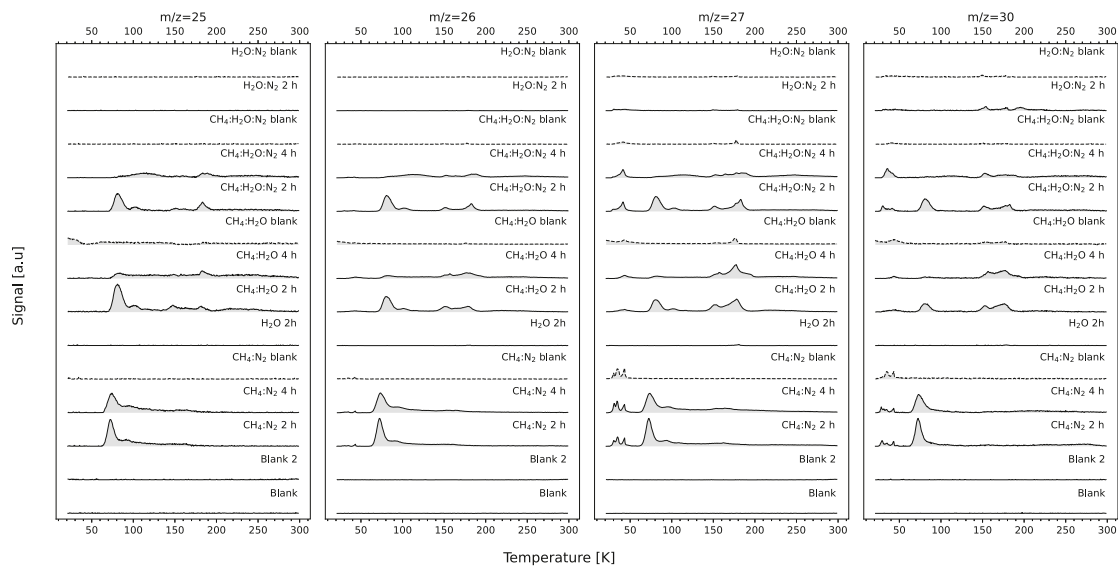


**Fig. B.16.** Compilation of the signals for  $\text{C}_2\text{H}_x$ , including additional measurements not included in the main text. All measurements are plotted on the same scale and the measurements have been offset from each other. The  $\text{H}_2\text{O}$  2 h irradiation was performed to see if there was any influence of potential hydrocarbons originating from the electron gun filament, which showed that a potential effect could be neglected. Similarly, the  $\text{H}_2\text{O}:\text{N}_2$  experiment was conducted to check a similar effect. For each irradiation experiment a corresponding blank was performed to distinguish irradiation products from any contamination in the gases or in the chamber. Though  $m/z = 28$  could correspond to a potential  $\text{C}_2\text{H}_4$  signal, the result was omitted because in experiments containing  $\text{N}_2$ ,  $m/z = 28$  largely corresponds to  $\text{N}_2$ , same with  $m/z = 29$ . Two complete blanks were performed, where the non-irradiated sample holder was heated up from 20 to 300 K and the desorption monitored. The experiment *Blank 2* was performed after a cable on the diode was fixed to check if the repair had introduced any noticeable contamination. Only a small contribution to  $m/z = 44$  from *Blank 2* was observed for  $T > 250$  K.

for their help in constructing the setup. Furthermore, the authors want to thank Adrian Etter for his help. The authors want to thank the two anonymous reviewers, whose comments were greatly appreciated and have improved the quality of the manuscript

## Appendix A. Irradiation

In this section, additional figures for the irradiation are provided. In Figs. A.12 and A.13 the calibration measurements for the electron gun are shown, the resulting values resulting in a current of  $1 \mu\text{A}$  were used

consistently in the measurement campaign. Fig. A.14 shows the QMS measurements during the irradiation of various ice samples. The irradiation of the additional measurements on pure  $\text{H}_2\text{O}$  and  $\text{H}_2\text{O}:\text{N}_2$  ices have been included in this section, but are not shown in the main text.

## Appendix B. Additional desorption plots

In this section, additional desorption measurement results are presented. Fig. B.15 shows the behavior of the main ice components of each mixture during the TPD and highlights their differences.

Table C.4

The electron ionization fragmentation pattern for the molecules used to fit the contributions in Figs. 7 and 9. The values have been taken from the NIST database (<http://webbook.nist.gov>). The highest respective peak is denoted by 9999 and the other values are normalized with respect to this peak.

m/z	Ethane	Ethylene	Acetylene	Hydrogen cyanide	Propane	Cyclopropane	Propene	Carbon dioxide	Ketene	Formaldehyde	Cyclopropene
24	50	230	500	0	10	30	30	0	440	0	212
25	350	781	1912	0	50	180	180	0	581	0	299
26	2322	5295	9999	1682	911	1271	1051	0	160	0	678
27	3323	6236	220	9999	4194	3503	3873	0	10	0	547
28	9999	9999	10	170	5875	250	140	981	1131	2400	0
29	2152	230	0	10	9999	10	0	10	681	9999	518
30	2622	10	0	0	220	0	0	0	10	5800	75
37	0	0	0	0	300	991	1271	0	0	0	2768
38	0	0	0	0	530	1441	1942	0	0	0	4669
39	0	0	0	0	1892	6726	7257	0	0	0	9999
40	0	0	0	0	280	3143	2913	0	510	0	6863
41	0	0	0	0	1341	8878	9999	0	2652	0	1036
42	0	0	0	0	601	9999	7036	0	9398	0	651
43	0	0	0	0	2312	330	230	0	210	0	54
44	0	0	0	0	2742	10	10	9999	10	0	0

Fig. B.16 shows the signals for  $m/z = 25, 26, 27,$  and  $30$  for all measurements conducted, including additional measurements. This shows that the  $C_2H_x$  signals originate from the processing of the ice and are not introduced by the electron gun.

### Appendix C. Fragmentation patterns

The fragmentation patterns from the NIST database (<http://webbook.nist.gov>), which were used to fit the contributions in Figs. 7 and 9, are collected in Table C.4.

### References

- Abplanalp, M.J., Góbi, S., Kaiser, R.I., 2019. On the formation and the isomer specific detection of methylacetylene ( $CH_3CCH$ ), propene ( $CH_3CHCH_2$ ), cyclopropane ( $c-C_3H_6$ ), vinylacetylene ( $CH_2CHCCH$ ), and 1, 3-butadiene ( $CH_2CHCHCH_2$ ) from interstellar methane ice analogues. *Phys. Chem. Chem. Phys.* 21, 5378–5393. <http://dx.doi.org/10.1039/C8CP03921F>.
- Abplanalp, M.J., Jones, B.M., Kaiser, R.I., 2018. Untangling the methane chemistry in interstellar and solar system ices toward ionizing radiation: A combined infrared and reflectron time-of-flight analysis. *Phys. Chem. Chem. Phys.* 20, 5435–5468. <http://dx.doi.org/10.1039/C7CP05882A>.
- Altwegg, K., Balsiger, H., Fuselier, S.A., 2019. Cometary chemistry and the origin of icy solar system bodies: The view after Rosetta. *Annu. Rev. Astron. Astrophys.* 57 (1), 113–155. <http://dx.doi.org/10.1146/annurev-astro-091918-104409>.
- Angell, C., 2004. Amorphous water. *Annu. Rev. Phys. Chem.* 55, 559–583. <http://dx.doi.org/10.1146/annurev-physchem.55.091602.094156>.
- Arumainayagam, C., Garrod, R., Boyer, M., Hay, A., Bao, S., Campbell, J., Wang, J., Nowak, C., Arumainayagam, M., Hodge, P., 2019. Extraterrestrial prebiotic molecules: photochemistry vs. radiation chemistry of interstellar ices. *Chem. Soc. Rev.* 48, <http://dx.doi.org/10.1039/C7CS00443E>.
- Bar-Nun, A., Herman, G., Laufer, D., Rappaport, M., 1985. Trapping and release of gases by water ice and implications for icy bodies. *Icarus* 63 (3), 317–332. [http://dx.doi.org/10.1016/0019-1035\(85\)90048-X](http://dx.doi.org/10.1016/0019-1035(85)90048-X), URL <https://www.sciencedirect.com/science/article/pii/001910358590048X>.
- Behrard, A., Fayolle, E.C., Graninger, D.M., Bergner, J.B., Martín-Doménech, R., Maksyutenko, P., Rajappan, M., Öberg, K.I., 2019. Desorption kinetics and binding energies of small hydrocarbons. *Astrophys. J.* 875 (1), 73. <http://dx.doi.org/10.3847/1538-4357/ab0e7b>.
- Bennett, C.J., Jamieson, C.S., Osamura, Y., Kaiser, R.I., 2006. Laboratory studies on the irradiation of methane in interstellar, cometary, and solar system ices. *Astrophys. J.* 653 (1), 792–811. <http://dx.doi.org/10.1086/508561>.
- Bennett, C.J., Kaiser, R.I., 2007. On the formation of glycolaldehyde ( $HCOCH_2OH$ ) and methyl formate ( $HCOOCH_3$ ) in interstellar ice analogs. *Astrophys. J.* 661 (2), 899–909. <http://dx.doi.org/10.1086/516745>.
- Bergner, J.B., Rajappan, M., Öberg, K.I., 2022. HCN snow lines in protoplanetary disks: Constraints from ice desorption experiments. *Astrophys. J.* 933 (2), 206. <http://dx.doi.org/10.3847/1538-4357/ac771e>.
- Boogert, A.A., Gerakines, P.A., Whittet, D.C., 2015. Observations of the icy universe. *Annu. Rev. Astron. Astrophys.* 53 (1), 541–581. <http://dx.doi.org/10.1146/annurev-astro-082214-122348>.
- Bossa, J.-B., Paardekooper, D., Isokoski, K., Linnartz, H., 2015. Methane ice photochemistry and kinetic study using laser desorption time-of-flight mass spectrometry at 20 K. *Phys. Chem. Chem. Phys.* 17, <http://dx.doi.org/10.1039/C5CP00578G>.
- Brooke, T.Y., Tokunaga, A.T., Weaver, H.A., Crovisier, J., Bockelée-Morvan, D., Crisp, D., 1996. Detection of acetylene in the infrared spectrum of comet hyakutake. *Nature* 383 (6601), 606–608. <http://dx.doi.org/10.1038/383606a0>.
- Brown, M.E., Schaller, E.L., Blake, G.A., 2015. Irradiation products on dwarf planet makemake. *Astron. J.* 149 (3), 105. <http://dx.doi.org/10.1088/0004-6256/149/3/105>.
- Collings, M.P., Anderson, M.A., Chen, R., Dever, J.W., Viti, S., Williams, D.A., McCoustra, M.R.S., 2004. A laboratory survey of the thermal desorption of astrophysically relevant molecules. *Mon. Not. R. Astron. Soc.* 354 (4), 1133–1140. <http://dx.doi.org/10.1111/j.1365-2966.2004.08272.x>.
- Combe, J.P., Singh, S., Johnson, K.E., McCord, T.B., De Sanctis, M.C., Ammannito, E., Carozzo, F.G., Ciarniello, M., Frigeri, A., Raponi, A., Tosi, F., Zambon, F., Scully, J.E., Raymond, C.A., Russell, C.T., 2019. The surface composition of Ceres' Ezinu quadrangle analyzed by the Dawn mission. *Icarus* 318, 124–146. <http://dx.doi.org/10.1016/j.icarus.2017.12.039>, URL <https://www.sciencedirect.com/science/article/pii/S0019103517308163>, The Composition of Ceres.
- Cooper, J.F., Christian, E.R., Richardson, J.D., Wang, C., 2003. Proton irradiation of centaur, kuiper belt, and oort cloud objects at plasma to cosmic ray energy. *Earth Moon Planets* 92 (1), 261–277. <http://dx.doi.org/10.1023/B:MOON.0000031944.41883.80>.
- Cooper, J.F., Johnson, R.E., Mauk, B.H., Garrett, H.B., Gehrels, N., 2001. Energetic ion and electron irradiation of the icy galilean satellites. *Icarus* 149 (1), 133–159.
- Corazzi, M.A., Brucato, J.R., Poggiali, G., Podio, L., Fedele, D., Codella, C., 2021. Thermal desorption of astrophysically relevant ice mixtures of acetaldehyde and acetonitrile from olivine dust. *Astrophys. J.* 913 (2), 128. <http://dx.doi.org/10.3847/1538-4357/abf6d3>.
- Coustenis, A., Salama, A., Schulz, B., Ott, S., Lellouch, E., Encrenaz, T.h., Gautier, D., Feuchtgruber, H., 2003. Titan's atmosphere from ISO mid-infrared spectroscopy. *Icarus* 161 (2), 383–403. [http://dx.doi.org/10.1016/S0019-1035\(02\)00028-3](http://dx.doi.org/10.1016/S0019-1035(02)00028-3).
- Cruikshank, D.P., Owen, T.C., Ore, C.D., Geballe, T.R., Roush, T.L., de Bergh, C., Sandford, S.A., Poulet, F., Benedix, G.K., Emery, J.P., 2005. A spectroscopic study of the surfaces of Saturn's large satellites:  $H_2O$  ice, tholins, and minor constituents. *Icarus* 175 (1), 268–283. <http://dx.doi.org/10.1016/j.icarus.2004.09.003>, URL <https://www.sciencedirect.com/science/article/pii/S0019103504002970>.
- Davis, M.R., Meier, R.M., Cooper, J.F., Loeffler, M.J., 2021. The contribution of Electrons to the sputter-produced  $O_2$  exosphere on Europa. *Astrophys. J. Lett.* 908 (2), L53. <http://dx.doi.org/10.3847/2041-8213/abe415>.
- d'Hendecourt, L., Allamandola, L., Greenberg, J., 1985. Time dependent chemistry in dense molecular clouds. I-Grain surface reactions, gas/grain interactions and infrared spectroscopy. *Astron. Astrophys.* 152, 130–150.
- Douté, S., Schmitt, B., Quirico, E., Owen, T.C., Cruikshank, D.P., de Bergh, C., Geballe, T.R., Roush, T.L., 1999. Evidence for methane segregation at the surface of pluto. *Icarus* 142 (2), 421–444. <http://dx.doi.org/10.1006/icar.1999.6226>.
- Drouin, D., Couture, A.R., Joly, D., Tastet, X., Aimez, V., Gauvin, R., 2007. CASINO V2.42—A fast and easy-to-use modeling tool for scanning electron microscopy and microanalysis users. *Scanning* 29 (3), 92–101. <http://dx.doi.org/10.1002/sca.20000>, <https://onlinelibrary.wiley.com/doi/abs/10.1002/sca.20000>.
- Esmaili, S., Bass, A.D., Cloutier, P., Sanche, L., Huels, M.A., 2018. Glycine formation in  $CO_2:CH_4:NH_3$  ices induced by 0-70 eV electrons. *J. Chem. Phys.* 148 (16), 164702. <http://dx.doi.org/10.1063/1.5021596>.
- Ferrari, B.C., Slavicinska, K., Bennett, C.J., 2021. Role of suprathermal chemistry on the evolution of carbon oxides and organics within interstellar and cometary ices. *Acc. Chem. Res.* 54 (5), 1067–1079. <http://dx.doi.org/10.1021/acs.accounts.0c00731>.
- Förstel, M., Bergantini, A., Maksyutenko, P., Góbi, S., Kaiser, R., 2017. Formation of methylamine and ethylamine in extraterrestrial ices and their role as fundamental building blocks of proteinogenic  $\alpha$ -amino acids. *Astrophys. J.* 845, 83. <http://dx.doi.org/10.3847/1538-4357/aa7edd>.

- Förstel, M., Maksyutenko, P., Jones, B.M., Sun, B.J., Chang, A.H.H., Kaiser, R.I., 2016. Synthesis of urea in cometary model ices and implications for comet 67P/Churyumov-Gerasimenko. *Chem. Commun.* 52, 741–744. <http://dx.doi.org/10.1039/C5CC007635H>.
- Galli, A., Vorbürger, A., Wurz, P., Pommerol, A., Cerubini, R., Jost, B., Poch, O., Tulej, M., Thomas, N., 2018. 0.2 To 10 keV electrons interacting with water ice: Radiolysis, sputtering, and sublimation. *Planet. Space Sci.* 155, 91–98. <http://dx.doi.org/10.1016/j.pss.2017.11.016>, URL <https://www.sciencedirect.com/science/article/pii/S0032063317301290>, Surfaces, atmospheres and magnetospheres of the outer planets, their satellites and ring systems: Part XII.
- Gibb, E., Mumma, M., Dello Russo, N., DiSanti, M., Magee-Sauer, K., 2003. Methane in oort cloud comets. *Icarus* 165 (2), 391–406. [http://dx.doi.org/10.1016/S0019-1035\(03\)00201-X](http://dx.doi.org/10.1016/S0019-1035(03)00201-X), URL <https://www.sciencedirect.com/science/article/pii/S001910350300201X>.
- Grundy, W.M., Binzel, R.P., Buratti, B.J., Cook, J.C., Cruikshank, D.P., Ore, C.M.D., Earle, A.M., Ennico, K., Howett, C.J.A., Lunsford, A.W., Olkin, C.B., Parker, A.H., Philippe, S., Protopapa, S., Quirico, E., Reuter, D.C., Schmitt, B., Singer, K.N., Verbiscer, A.J., Beyer, R.A., Buie, M.W., Cheng, A.F., Jennings, D.E., Linscott, I.R., Parker, J.W., Schenk, P.M., Spencer, J.R., Stansberry, J.A., Stern, S.A., Throop, H.B., Tsang, C.C.C., Weaver, H.A., Weigle, G.E., Young, L.A., null null, 2016. Surface compositions across pluto and charon. *Science* 351 (6279), aad9189. <http://dx.doi.org/10.1126/science.aad9189>, <https://www.science.org/doi/abs/10.1126/science.aad9189>.
- Grundy, W.M., Young, L.A., Stansberry, J.A., Buie, M.W., Olkin, C.B., Young, E.F., 2010. Near-infrared spectral monitoring of triton with IRTF/SpEx II: Spatial distribution and evolution of ices. *Icarus* 205 (2), 594–604. <http://dx.doi.org/10.1016/j.icarus.2009.08.005>.
- Gudipati, M.S., Cooper, P.D., 2013. Chemistry in water ices: From fundamentals to planetary applications. In: Gudipati, M.S., Castillo-Rogez, J. (Eds.), *The Science of Solar System Ices*. Springer New York, New York, NY, pp. 503–526. [http://dx.doi.org/10.1007/978-1-4614-3076-6\\_15](http://dx.doi.org/10.1007/978-1-4614-3076-6_15).
- Hansen, C.J., Castillo-Rogez, J., Grundy, W., Hofgartner, J.D., Martin, E.S., Mitchell, K., Nimmo, F., Nordheim, T.A., Paty, C., Quick, L.C., Roberts, J.H., Runyon, K., Schenk, P., Stern, A., Umurhan, O., 2021. Triton: Fascinating moon, likely ocean world, compelling destination!. *Planet. Sci. J.* 2 (4), 137. <http://dx.doi.org/10.3847/PSJ/abffd2>.
- Holtom, P., Bennett, C., Osamura, Y., Mason, N., Kaiser, R., 2005. A combined experimental and theoretical study on the formation of the amino acid glycine (NH<sub>2</sub>CH<sub>2</sub>COOH) and its isomer (CH<sub>3</sub>NHCOOH) in extraterrestrial ICES. *Astrophys. J.* 626, 940. <http://dx.doi.org/10.1086/430106>.
- Hudson, R.L., Moore, M.H., Raines, L.L., 2009. Ethane ices in the outer solar system: Spectroscopy and chemistry. *Icarus* 203 (2), 677–680. <http://dx.doi.org/10.1016/j.icarus.2009.06.026>.
- Hudson, R.L., Palumbo, M.E., Strazzulla, G., Moore, M.H., Cooper, J.F., Sturmer, S.J., 2008. Laboratory studies of the chemistry of transneptunian object surface materials. In: Barucci, M.A., Boehnhardt, H., Cruikshank, D.P., Morbidelli, A., Dotson, R. (Eds.), *The Solar System beyond Neptune*. pp. 507–523.
- Jones, B.M., Kaiser, R.I., Strazzulla, G., 2014. UV-VIS, infrared, and mass spectroscopy of electron irradiated frozen oxygen and carbon dioxide mixtures with water. *Astrophys. J.* 781 (2), 85. <http://dx.doi.org/10.1088/0004-637x/781/2/85>.
- Jones, E., Oliphant, T., Peterson, P., et al., 2001. SciPy: Open source scientific tools for Python. URL <http://www.scipy.org/>.
- Kaiser, R.I., Maity, S., Jones, B.M., 2015. Synthesis of prebiotic glycerol in interstellar ices. *Angew. Chem. Int. Ed.* 54 (1), 195–200.
- Kaiser, R.I., Stockton, A.M., Kim, Y.S., Jensen, E.C., Mathies, R.A., 2013. On the formation of dipeptides in interstellar model ices. *Astrophys. J.* 765 (2), 111. <http://dx.doi.org/10.1088/0004-637x/765/2/111>.
- Kim, Y.S., Kaiser, R.I., 2012. Electron irradiation of kuiper belt surface ices: Ternary n<sub>2</sub>-CH<sub>4</sub>-CO mixtures as a case study. *Astrophys. J.* 758 (1), 37. <http://dx.doi.org/10.1088/0004-637x/758/1/37>.
- Ligterink, N.F.W., Coutens, A., Kofman, V., Müller, H.S.P., Garrod, R.T., Calcutt, H., Wampfler, S.F., Jørgensen, J.K., Linnartz, H., van Dishoeck, E.F., 2017. The ALMA-PILS survey: detection of CH<sub>3</sub>NCO towards the low-mass protostar IRAS 16293-2422 and laboratory constraints on its formation. *Mon. Not. R. Astron. Soc.* 469 (2), 2219–2229. <http://dx.doi.org/10.1093/mnras/stx890>.
- Ligterink, N.F.W., Terwisscha van Scheltinga, J., Taquet, V., Jørgensen, J.K., Cazaux, S., van Dishoeck, E.F., Linnartz, H., 2018. The formation of peptide-like molecules on interstellar dust grains. *Mon. Not. R. Astron. Soc.* 480 (3), 3628–3643. <http://dx.doi.org/10.1093/mnras/sty2066>.
- Luu, J., Jewitt, D., 1996. Color diversity among the centaurs and kuiper belt objects. *Astron. J.* 112, 2310. <http://dx.doi.org/10.1086/118184>.
- Marks, J.H., Wang, J., Fortenberry, R.C., Kaiser, R.I., 2022. Preparation of methanediamine (CH<sub>2</sub>(NH<sub>2</sub>)<sub>2</sub>) - A precursor to nucleobases in the interstellar medium. *Proc. Natl. Acad. Sci.* 119 (51), e2217329119. <http://dx.doi.org/10.1073/pnas.2217329119>, <https://www.pnas.org/doi/abs/10.1073/pnas.2217329119>.
- Mason, N., Nair, B., Jheeta, S., Szymańska, E., 2014. Electron induced chemistry: A new frontier in astrochemistry. *Faraday Discuss.* 168, <http://dx.doi.org/10.1039/c4fd00004h>.
- Materese, C.K., Cruikshank, D.P., Sandford, S.A., Imanaka, H., Nuevo, M., 2015. Ice chemistry on outer solar system bodies: Electron radiolysis of N<sub>2</sub>, CH<sub>4</sub>, and CO-containing ices. *Astrophys. J.* 812 (2), 150. <http://dx.doi.org/10.1088/0004-637x/812/2/150>.
- Meier, R.M., Loeffler, M.J., 2020. Sputtering of water ice by kev electrons at 60 K. *Surf. Sci.* 691, 121509. <http://dx.doi.org/10.1016/j.susc.2019.121509>, URL <https://www.sciencedirect.com/science/article/pii/S0039602819304613>.
- Mífusd, D., Juhász, Z., Herczku, P., Kovács, S., Ioppolo, S., Kanuchova, Z., Czentye, M., Hailey, P., Traspas, A., Mason, N., McCullough, R., Paripás, B., Sulik, B., 2021. Electron irradiation and thermal chemistry studies of interstellar and planetary ice analogues at the ICA astrochemistry facility. *Eur. Phys. J. D* 75, <http://dx.doi.org/10.1140/epjd/s10053-021-00192-7>.
- Moore, M., Hudson, R., 2003. Infrared study of ion-irradiated N<sub>2</sub>-dominated ices relevant to triton and pluto: formation of HCN and HNC. *Icarus* 161 (2), 486–500. [http://dx.doi.org/10.1016/S0019-1035\(02\)00037-4](http://dx.doi.org/10.1016/S0019-1035(02)00037-4), URL <https://www.sciencedirect.com/science/article/pii/S0019103502000374>.
- Morbidelli, A., Bitsch, B., Crida, A., Gounelle, M., Guillot, T., Jacobson, S., Johansen, A., Lambrechts, M., Lega, E., 2016. Fossilized condensation lines in the solar system protoplanetary disk. *Icarus* 267, 368–376. <http://dx.doi.org/10.1016/j.icarus.2015.11.02710.48550/arXiv.1511.06556>.
- Müller, D.R., Altwegg, K., Berthelier, J.J., Combi, M., De Keyser, J., Fuselier, S.A., Hänni, N., Pestoni, B., Rubin, M., Schroeder, I.R.H.G., Wampfler, S.F., 2022. High D/H ratios in water and alkanes in comet 67P/Churyumov-Gerasimenko measured with Rosetta/ROSINA DFMS. *A & A* 662, A69. <http://dx.doi.org/10.1051/0004-6361/202142922>.
- Mumma, M.J., DiSanti, M.A., Russo, N.D., Fomenkova, M., Magee-Sauer, K., Kaminski, C.D., Xie, D.X., 1996. Detection of abundant ethane and methane, along with carbon monoxide and water, in comet C/1996 B2 hyakutake: Evidence for interstellar origin. *Science* 272 (5266), 1310–1314, URL <http://www.jstor.org/stable/2889791>.
- Owen, T.C., Roush, T.L., Cruikshank, D.P., Elliot, J.L., Young, L.A., de Bergh, C., Schmitt, B., Geballe, T.R., Brown, R.H., Bartholomew, M.J., 1993. Surface ices and the atmospheric composition of pluto. *Science* 261 (5122), 745–748. <http://dx.doi.org/10.1126/science.261.5122.745>, <https://www.science.org/doi/abs/10.1126/science.261.5122.745>.
- Perna, D., Hromakina, T., Merlin, F., Ieva, S., Fornasier, S., Belskaya, I., Mazzotta Epifani, E., 2016. The very homogeneous surface of the dwarf planet makemake. *Mon. Not. R. Astron. Soc.* 466 (3), 3594–3599. <http://dx.doi.org/10.1093/mnras/stw3272>.
- Prockter, L., 2005. Ice in the solar system. *Johns Hopkins APL Tech. Dig.* 26.
- Qasim, D., Fedoseev, G., Chuang, K.J., He, J., Ioppolo, S., van Dishoeck, E.F., Linnartz, H., 2020. An experimental study of the surface formation of methane in interstellar molecular clouds. *Nat. Astron.* 4, 781–785. <http://dx.doi.org/10.1038/s41550-020-1054-y>.
- Quirico, E., Douté, S., Schmitt, B., de Bergh, C., Cruikshank, D.P., Owen, T.C., Geballe, T.R., Roush, T.L., 1999. Composition, physical state, and distribution of ices at the surface of triton. *Icarus* 139 (2), 159–178. <http://dx.doi.org/10.1006/icar.1999.6111>.
- Raut, U., Teolis, B.D., Kammer, J.A., Gimar, C.J., Brody, J.S., Gladstone, G.R., Howett, C.J.A., Protopapa, S., Retherford, K.D., 2022. Charon's refractory factory. *Sci. Adv.* 8 (24), eabq5701. <http://dx.doi.org/10.1126/sciadv.abq5701>, <https://www.science.org/doi/abs/10.1126/sciadv.abq5701>.
- Renner, T., 2007. In: Cohen, E.R., Cvitas, T., Frey, J.G., Holstr (Eds.), *Quantities, Units and Symbols in Physical Chemistry*, 3rd edition. The Royal Society of Chemistry, <http://dx.doi.org/10.1039/9781847557889>.
- Rowntree, P., Parenteau, L., Sanche, L., 1991. Electron stimulated desorption via dissociative attachment in amorphous H<sub>2</sub>O. *J. Chem. Phys.* 94 (12), 8570–8576. <http://dx.doi.org/10.1063/1.460090>.
- Rubin, M., Bekaert, D.V., Broadley, M.W., Drozdovskaya, M.N., Wampfler, S.F., 2019. Volatile species in comet 67P/Churyumov-Gerasimenko: Investigating the link from the ISM to the terrestrial planets. *ACS Earth Space Chem.* 3 (9), 1792–1811. <http://dx.doi.org/10.1021/acsearthspacechem.9b00096>.
- Sagan, C., Khare, B., 1979. *Tholins: Organic chemistry of interstellar grains and gas. Nature* 277, 102–107.
- Satorre, M., Domingo, M., Millán, C., Luna, R., Vilaplana, R., Santonja, C., 2008. Density of CH<sub>4</sub>, N<sub>2</sub> and CO<sub>2</sub> ices at different temperatures of deposition. *Planet. Space Sci.* 56 (13), 1748–1752. <http://dx.doi.org/10.1016/j.pss.2008.07.015>.
- Sullivan, K.K., Boamah, M.D., Shulenberg, K.E., Chapman, S., Atkinson, K.E., Boyer, M.C., Arumainayagam, C.R., 2016. Low-energy (<20 eV) and high-energy (1000 eV) electron-induced methanol radiolysis of astrochemical interest. *Mon. Not. R. Astron. Soc.* 460 (1), 664–672. <http://dx.doi.org/10.1093/mnras/stw593>.
- Tegler, S.C., Cornelison, D.M., Grundy, W.M., Romanishin, W., Abernathy, M.R., Bovyn, M.J., Burt, J.A., Evans, D.E., Maleszewski, C.K., Thompson, Z., Vilas, F., 2010. Methane and nitrogen abundances on pluto and eris. *Astrophys. J.* 725 (1), 1296–1305. <http://dx.doi.org/10.1088/0004-637x/725/1/1296>.
- Virtanen, P., Gommers, R., Oliphant, T.E., Haberland, M., Reddy, T., Cournapeau, D., Burovski, E., Peterson, P., Weckesser, W., Bright, J., van der Walt, S.J., Brett, M., Wilson, J., Millman, K.J., Mayorov, N., Nelson, A.R.J., Jones, E., Kern, R., Larson, E., Carey, C.J., Polat, I., Feng, Y., Moore, E.W., VanderPlas, J., Laxalde, D., Perktold, J., Cimrman, R., Henriksen, I., Quintero, E.A., Harris, C.R.,

- Archibald, A.M., Ribeiro, A.H., Pedregosa, F., van Mulbregt, P., SciPy 1.0 Contributors, 2020. SciPy 1.0: Fundamental algorithms for scientific computing in python. *Nature Methods* 17, 261–272. <http://dx.doi.org/10.1038/s41592-019-0686-2>.
- Wilson, P.D., Sagan, C., Thompson, W.R., 1994. The organic surface of 5145 pholus: Constraints set by scattering theory. *Icarus* 107 (2), 288–303.
- Wright, I.P., Sheridan, S., Barber, S.J., Morgan, G.H., Andrews, D.J., Morse, A.D., 2015. CHO-bearing organic compounds at the surface of 67P/Churyumov-Gerasimenko revealed by ptolemy. *Science* 349 (6247), aab0673. <http://dx.doi.org/10.1126/science.aab0673>, <https://www.science.org/doi/abs/10.1126/science.aab0673>.
- Wu, Y.-J., Wu, C.Y.R., Chou, S.-L., Lin, M.-Y., Lu, H.-C., Lo, J.-I., Cheng, B.-M., 2012. Spectra and photolysis of pure nitrogen and methane dispersed in solid nitrogen with vacuum-ultraviolet light. *Astrophys. J.* 746 (2), 175. <http://dx.doi.org/10.1088/0004-637X/746/2/175>.
- Wyckoff, R.W.G., Wyckoff, R.W., 1965. *Crystal Structures* 4, Vol. 1. Interscience publishers New York.
- Zhang, Z.M., Chen, S., Liang, Y.Z., 2010. Baseline correction using adaptive iteratively reweighted penalized least squares. *Analyst* 135, 1138–1146. <http://dx.doi.org/10.1039/B922045C>.
- Zheng, W., Jewitt, D., Kaiser, R.L., 2006. Formation of hydrogen, oxygen, and hydrogen peroxide in electron-irradiated crystalline water ice. *Astrophys. J.* 639 (1), 534–548. <http://dx.doi.org/10.1086/499231>.
- Zheng, W., Jewitt, D., Kaiser, R., 2009. On the state of water ice on saturn's moon titan and implications to icy bodies in the outer solar system. *J. Phys. Chem. A* 113, 11174–11181. <http://dx.doi.org/10.1021/jp903817y>.
- Zheng, W., Kaiser, R.L., 2010. Formation of hydroxylamine (NH<sub>2</sub>OH) in electron-irradiated ammonia-water ices. *J. Phys. Chem. A* 114 (16), 5251–5255. <http://dx.doi.org/10.1021/jp911946m>.